

University of Warwick institutional repository: <http://go.warwick.ac.uk/wrap>

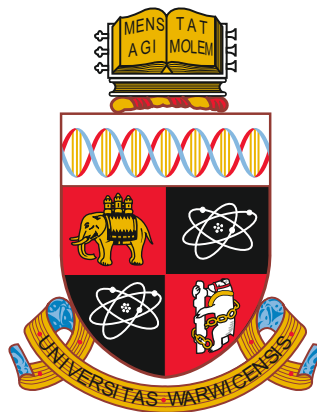
A Thesis Submitted for the Degree of PhD at the University of Warwick

<http://go.warwick.ac.uk/wrap/55918>

This thesis is made available online and is protected by original copyright.

Please scroll down to view the document itself.

Please refer to the repository record for this item for information to help you to cite it. Our policy information is available from the repository home page.



Fabrication of high temperature piezoelectric ceramics by sol gel method

Kevin McAughey

A thesis submitted to the
University of Warwick for the
degree of Master of Science

Department of Physics

THE UNIVERSITY OF
WARWICK

April 2011

Contents

List of Figures and Tables	v
Acknowledgments	ix
Declaration	x
Abstract	xi
1. Introduction	1
1.1. High Temperature Applications	1
1.2. NDT Techniques	2
1.2.1. Thermography	2
1.2.2. Eddy Current Techniques	3
1.2.3. Ultrasound	5
1.2.3.1. Electromagnetic Acoustic Transducers	5
1.2.3.2. Laser Ultrasound	8
1.2.3.3. Piezoelectric Transducers	9
References	13
2. Production and Operation of Piezoelectric Transducers	18
2.1. Sol Gel Techniques	18

2.2. The Piezoelectric Effect	22
2.2.1. Tensor Treatment of Piezoelectricity	24
2.2.2. Piezoelectric Effect in Bismuth Titanate	28
2.3. Ultrasound Propagation	29
2.3.1. Ultrasonic Transducers	30
2.3.2. Ultrasonic Waves	31
2.3.3. Attenuation of Bulk Waves	33
2.3.4. Transmission of Ultrasound Between Media	34
2.3.5. Using Ultrasound for Thickness Testing	36
References	39
3. Material Characterisation Techniques	41
3.1. Thermal Characterisation	41
3.2. Crystallographic Characterisation	42
References	44
4. Experimental Techniques Developed for Preparing Bismuth Titanate Transducers	45
4.1. Sample preparation	45
4.1.1. First preparation; TiP/BiN AcA	46
4.1.2. Second preparation; TiP/BiN NiA(+H ₂ O)	47
4.1.3. Third preparation; TiP/BiN AyA	48
4.2. Poling	50
4.2.1. Furnace Poling	50
4.2.2. Oil-Bath Poling	53

4.3. Fabrication and Characterisation of Thick Films	55
References	56
5. Characterisation of Bismuth Titanate Samples Produced Using Sol Gel Techniques	58
5.1. Thermal Characterisation	58
5.1.1. Thermogravimetric Analysis	58
5.1.2. Differential Scanning Calorimetry	61
5.2. Crystal Characterisation using X-ray Diffraction	65
5.2.1. Room Temperature X-ray Powder Diffractometry	67
5.2.2. High Temperature X-ray Powder Diffractometry	75
5.3. Optical Characterisation Results	79
References	82
6. Characterisation of the Ultrasonic Behaviour of Bismuth Titanate Samples	83
6.1. Tap Test Measurements	83
6.2. Use of the Sample Transducer for the Generation and Detection of Ultrasound	85
6.2.1. Aluminium Test Block Thickness Measurements	88
6.2.2. Transducer Measurements	88
References	89
7. Conclusions	90
7.1. Results and Discussion	90
7.1.1. Material Characterisation	90

7.2. Evaluation of Novel Experimental Methods	91
7.2.1. Novel Sol Gel Method	91
7.2.2. Oil-Bath Poling	92
7.3. Future Investigations	93
7.3.1. Alternative Poling Methods	93
7.3.2. High Temperature Experiments	93
7.3.3. Thick Film Experiments	94
7.3.4. Doping	95
References	95

List of Figures

1. Introduction

Figure 1.1 (p. 4): A diagram of an Eddy Current Coil

Figure 1.2 (p. 6): A diagram of an EMAT

Figure 1.3 (p. 7): A diagram of magnetostriction

Figure 1.4 (p. 9): A diagram of a piezoelectric transducer

2. Production and Operation of Piezoelectric Transducers

Figure 2.1 (p. 19): A diagram of step and chain polymerisation

Figure 2.2 (p. 21): A diagram of the structure of a titanium complex

Figure 2.3 (p. 22): A diagram of a general condensation reaction

Figure 2.4 (p. 23): A diagram of the inverse piezoelectric effect

Figure 2.5 (p. 24): A diagram of the perovskite structure of barium titanate

Figure 2.6 (p. 28): A diagram of the structure of bismuth titanate

Figure 2.7 (p. 30): A diagram of harmonics in a piezoelectric transducer

Figure 2.8 (p. 31): A diagram of the propagation of longitudinal and shear waves

Figure 2.9 (p. 32): A diagram of the propagation of a Rayleigh wave

Figure 2.10 (p. 33): A diagram of the propagation of a Lamb wave

Figure 2.11 (p. 35): A diagram of the boundary between two media

Figure 2.12 (p. 37): A diagram of thickness gauging using ultrasound

Figure 2.13 (p. 38): A diagram of flaw detection using ultrasound

3. Material Characterisation Techniques

Figure 3.1 (p. 43): A diagram of the motion of an x-ray diffractometer

4. Experimental Techniques Developed for Preparing Bismuth Titanate Transducers

Figure 4.1 (p. 49): A photograph of a sol after being dried

Figure 4.2 (p. 51): A schematic of the furnace poling setup

Figure 4.3 (p. 53): A schematic of the oil-bath poling setup

5. Characterisation of Bismuth Titanate Samples Produced Using Sol Gel Techniques

Figure 5.1 (p. 59): A graph of the weight loss against temperature for the TiP/BiN NiA sample

Figure 5.2 (p. 60): A graph of the weight loss against temperature for the TiP/BiN NiA+H₂O sample

Figure 5.3 (p. 61): A graph of the heatflow against temperature for the TiP/BiN NiA sample

Figure 5.4 (p. 62): Enlargements of a graph of the heatflow against temperature for the TiP/BiN NiA sample

Figure 5.5 (p. 63): A graph of the heatflow against temperature for the TiP/BiN NiA+H₂O sample

Figure 5.6 (p. 64): Enlargements of a graph of the heatflow against temperature for the TiP/BiN NiA+H₂O sample

Figure 5.7 (p. 66): A graph showing the reference XRD pattern

- Figure 5.8 (p. 67): A graph showing the XRD pattern for the TiP/BiN AcA sample
- Figure 5.9 (p. 68): Enlargement showing peak splitting in the TiP/BiN AcA sample
- Figure 5.10 (p. 69): A graph showing the XRD pattern for the TiP/BiN NiA sample
- Figure 5.11 (p. 70): A graph showing the XRD pattern for the TiP/BiN NiA+H₂O sample
- Figure 5.12 (p. 71): A graph showing the XRD pattern for the TiP/BiN AyA sample
- Figure 5.13 (p. 73): A graph showing a comparison of the XRD pattern for the TiP/BiN AyA sample, the reference pattern and the XRD pattern of a commercial sample
- Figure 5.14 (p. 76): A graph showing a series of high temperature XRD patterns from 600°C to 700°C for the TiP/BiN AyA sample
- Figure 5.15 (p. 77): A graph showing a series of high temperature XRD patterns from 600°C to 700°C for the TiP/BiN AyA sample enlarged at a single peak
- Figure 5.16 (p. 78): A graph showing a series of high temperature XRD patterns from 660°C to 670°C for the TiP/BiN AyA sample
- Figure 5.17 (p. 79): A graph showing a series of high temperature XRD patterns from 660°C to 670°C for the TiP/BiN AyA sample enlarged at a single peak
- Figure 5.18 (p. 80): A diagram showing the thickness measurement of a film using an optical microscope
- Figure 5.19 (p. 81): Photographs showing the microscope focusing on the film and the substrate
- Figure 5.20 (p. 81): Photographs showing the microscope focusing on the film at extremities of thickness

6. Characterisation of the Ultrasonic Behaviour of Bismuth Titanate

Samples

Figure 6.1 (p. 83): A graph showing the amplitude response of a transducer to a tap test

Figure 6.2 (p. 84): A graph showing the frequency response of a transducer during a tap test

Figure 6.3 (p. 86): A schematic of the experimental transducer setup

Figure 6.4 (p. 87): A graph showing the amplitude response of two transducers during a thickness measurement

List of Tables

Table 1 (p 12): Table showing the Curie temperatures of piezoelectric materials

Table 2 (p 26): Table showing the relation between tensor notation and reduced notation

Table 3 (p 55): Table showing the firing temperatures of different zones in the belt furnace

Table 4 (p 74): Table showing the purity of the samples prepared in this research

Table 5 (p 75): Table showing the lattice parameters of the sample submitted for Rietveld refinement

Acknowledgments

I would like to thank all of the staff at the University of Warwick for all the help and guidance I have received. I would especially like to thank my supervisors Dr. Rachel Edwards and Dr. Susan Burrows, as well as Tom Orton and all the staff in the Electronics Workshop. I would also like to thank my family and friends for all of their support and patience.

Declaration

The research presented in this thesis, except where explicitly stated otherwise, is entirely that of the author. This research was carried out in the Department of Physics, University of Warwick, from October 2009 to September 2010.

No part of this thesis has been submitted to this, or any other, academic institution for admission to a higher degree. However, some of the work has been presented at a conference.

Abstract

This research covers the fabrication of piezoelectric ceramics using a sol gel method. Commercial high temperature transducers are typically fabricated by a milled oxide method. The sol gel method presented here produced purer samples that can be prepared at lower temperatures than conventional milled oxide preparations. The performance of the samples as piezoelectric transducers was also investigated, with the samples produced by sol gel method exceeding the piezoelectric response of the commercial samples.

1. Introduction

Non destructive testing (NDT) is a discipline that focuses on the evaluation of physical samples without causing damage or wear to the samples being examined [1-9]. It can also allow inspections to be carried out in-situ on components which are in active use [4], though in many cases machinery must be shut down to perform testing [5]. High temperature, usually above 200°C, non-destructive testing (HTNDT) is an expanding field which provides numerous advantages over ambient temperature NDT, but has many challenges as well [4, 6-9].

In situations such as those in factories and power plants the ability to examine components in real time, potentially at high temperature, allows critical safety checks to be carried out without reducing productivity or causing expensive shutdowns. In addition to these applications, more novel uses can be expected to develop as the field matures, such as permanently fixed flaw detection devices being placed inside jet turbines to allow maintenance checks to be carried out quickly and remotely.

In this research a new, low temperature method of preparing high temperature piezoelectric transducers has been developed. The transducers prepared using this method have also been characterised chemically and ultrasonically. These have the potential to be used at temperatures of over 500°C.

1.1 High Temperature Applications

High temperature NDT is extremely useful in several industries, such as the manufacturing industry, the power generation industry and the petrochemical industry, but the applications extend beyond those. In manufacturing of steel billet, for example, HTNDT allows products to be inspected early in the process, when

recycling of failed components is easier. This requires operating temperatures of up to 1000°C [10]. In the power generation industry HTNDT allows inspection of high temperature, high wear components, usually up to 550°C, without requiring expensive shutdowns. The petrochemical industry has similar requirements for high temperature inspection. The eventual goal of this research is to produce transducers capable of operating at up to 550°C, making it ideal for some of the industries described above. This value is limited by the type of piezoelectric material being investigated.

1.2 NDT Techniques

There are many different techniques used in NDT, each with advantages and disadvantages. The following is a brief summary of the more common methods which can be used, both at ambient temperature and in high temperature applications.

1.2.1 Thermography

Thermography uses the flow of heat in a material to detect and identify flaws [11]. There are two main subdivisions of thermography; active and passive. Active thermography involves the application of thermal energy to the sample being investigated. This is usually performed with high intensity lamps pulsed for a very brief period, followed by the monitoring of heat dissipation from the surface of the sample. A hotspot indicates an area where the heatflow is obstructed, for example by a void or an inclusion, or possibly a delamination in composite materials [12]. This technique is known as flash thermography. In recent research thermography been combined with another form of NDT, namely laser ultrasound, where the laser can be used as a source of ultrasound as well as a heat source [3]. The transmission of heat

through a metal is a well defined process, so if a sample is heated from a single point and the spread of heat measured using a thermal imaging camera, any anomalies in the pattern of the heatflow will be detected and assigned to the presence of defects or flaws. This method can accurately size and locate surface and bulk defects by analysing when a hotspot appears, and how large it is [11]. The remote nature of the technique means that it is well suited to high temperature measurements, with the effective operating temperature of the thermal imaging cameras ranging from -20 C to 2000 C [13].

In passive thermography no additional thermal energy is applied to the sample. In HTNDT this can be used to examine a high temperature component during operation to check for hotspots or coldspots, indicating operation outside of accepted parameters [11]. Passive thermography is also often used to examine the thermal efficiency of buildings.

1.2.2 Eddy Current Techniques

Eddy current testing uses electrical currents to examine the surface or near-surface of a material. A common setup of this method is shown in figure 1.1. Eddy current testing operates by passing an alternating current (AC) through a coil of wire. When held near an electrically conductive material induction will cause eddy currents to flow in the test material, as shown in figure 1.1 [14]. These currents can then be detected using a secondary search coil, by measuring the impact the eddy currents have on the primary generation coil, or by using a Hall probe, giant magnetoresistor or other sensor [14]. The penetration of eddy currents into a material is limited by the material's skin depth δ , the depth of penetration for electromagnetic radiation [15], as given by:

$$\delta = \sqrt{\frac{1}{\pi\mu_0\mu_r f\sigma}} \quad (1.1)$$

where μ_0 is the permeability of free space, μ_r is the relative permeability of the sample, σ is the electrical conductivity of the sample and f is the frequency of the signal. As the depth of detection is clearly limited by the frequency of the AC signal, this can be varied to examine different depths into the sample [16].

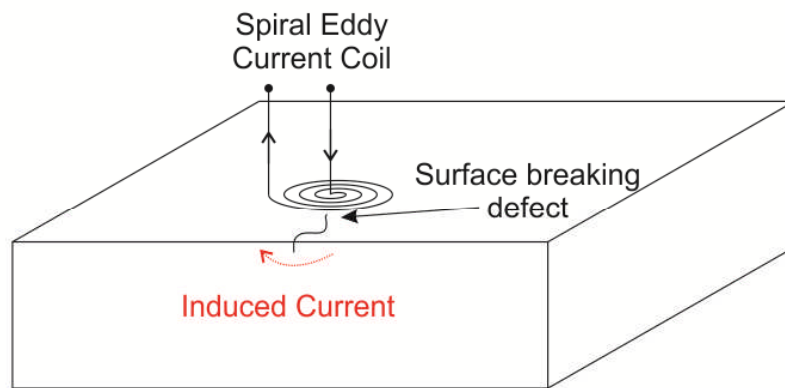


Figure 1.1. Eddy current coil and the effect of a defect. The coil creates an induced current in the sample, which is forced to flow under the surface breaking defect.

Alternatively, pulsed eddy currents can be used to overcome this requirement. In pulsed eddy current testing a step function AC signal is used instead of a sinusoidal AC signal [16]. This step function will contain many different frequencies and allows information from multiple depths to be collected simultaneously [15]. The non-contact nature of the technique makes it useful in high temperature applications, although the signal is sensitive to liftoff, limiting the distance the probe can be from the sample.

1.2.3 Ultrasound

One of the most widely used forms of NDT is ultrasonic testing, due to its versatility, simplicity and cost effectiveness. Ultrasound can be used to examine both the surface and the bulk of samples to find defects [17, Ch 5-9]. Thickness measurements can also be made using ultrasound for a range of samples, from sub-millimetre thick sheets such as those used in drinks cans manufacturing [18], to plates tens of centimetres thick used in ships [19]. The process of using ultrasound for NDT has no theoretical limit in terms of the behaviour of the sample at high temperature, although the melting point of the sample is usually an experimental limit. This limit, however, is usually far in excess of the temperature at which the ultrasound transducers are capable of generating and detecting the signals, as discussed below.

Ultrasonic transducers can be divided into two broad categories; contact and non-contact. Contact transducers are the most frequently used and commonly use simple piezoelectric elements. Contact methods typically have greater full cycle efficiency, from generation and detection efficiencies due to improved coupling when compared to non-contact techniques. Non-contact methods, such as laser ultrasound, are generally easier to use at high temperatures due to their ability to operate remotely from the sample and therefore at a standoff from the high temperature component [20], but these methods are not yet widely used in industry.

The following is a summary of some of the methods of ultrasound generation and detection.

1.2.3.1 Electromagnetic Acoustic Transducers

An electromagnetic acoustic transducer (EMAT) is a non-contact transducer for generating and/or detecting ultrasound in either electrically conducting materials,

magnetic materials, or materials which are both. They are usually composed of a permanent magnet and a coil of wire as shown in figure 1.2 [21].

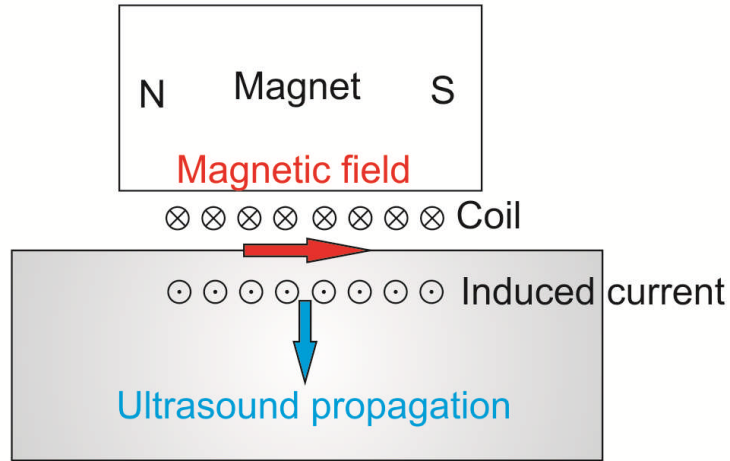


Figure 1.2. A diagram of an EMAT and the ultrasound it generates in the sample, shown as a blue arrow.

An alternating current, typically from a discharging capacitor, is pulsed through the coil, creating an induced current in the sample. For an electrically conducting material this acts in conjunction with the magnetic field to exert a Lorentz force \underline{F} on the electrons in the sample.

$$\underline{F} = q(\underline{v} \times \underline{B}) \quad (1.2)$$

where q is the charge of the electron, \underline{v} is its velocity and \underline{B} is the magnetic field. The force on the electron causes it move in the at right angles to both the magnetic field and current flow. The electrons move the lattice by the Coulomb attraction, causing the propagation of ultrasound [22]. The motion of the electrons corresponds to the electrical signal used to drive the EMAT coil. In EMAT detection the motion of the particles in the sample in a magnetic field causes a current to flow in the sample, which causes an induced current to flow in the coil. This current can then be detected

by an oscilloscope. Different arrangements of coils and magnetic fields will generate and detect different wavemodes of ultrasound [20].

In non-electrically conducting, magnetic materials, the ultrasound generation is by magnetostriction [23]. This effect is caused by the change in strain in a magnetic material when a magnetic field is applied to it, and is illustrated in figure 1.3. The changing magnetic field produced by the current flowing in the EMAT coil will cause a changing strain in the sample, causing the generation of ultrasound in the sample.

The distance of an EMAT from a sample, known as its liftoff, can affect the transducer's ability to generate or detect ultrasound of suitable amplitude in the sample. This is because as the sample moves further from the transducer the strength of the induced current in the sample and the static field decrease [24].

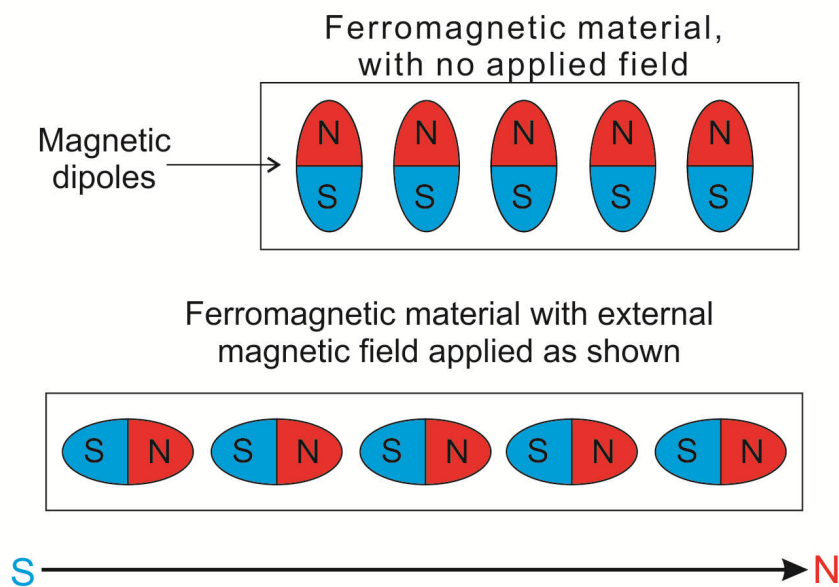


Figure 1.3. The effect of an applied field on a ferromagnetic material. Note the change in shape of the sample due to the rearrangement of the magnetic dipoles.

EMATs operating at high temperature are limited by the Curie temperature of the magnet used, for example, 300°C for a neodymium (NdFeB) magnet [25]. This is often overcome by using active cooling such as water cooling, although some recent work has focused on using a pulsed electromagnet [9], allowing higher temperatures to be reached without any active cooling.

1.2.3.2 Laser Ultrasound

Generation of ultrasound using a laser is a non-contact technique which uses a pulsed laser focused on a small spot on the sample. Laser generation of ultrasound works in two regimes; thermoelastic and ablative generation [26]. When operating in the thermoelastic regime the thermal expansion caused by heat in the sample due to the pulsed laser creates an ultrasound pulse in the sample. In this regime the sample is undamaged as the energy of the laser is conducted away from the point of generation as heat [27]. The ablative regime is not strictly speaking non-destructive due to the laser transmitting such high energy that a small portion of the surface is damaged by the laser [27]. The laser heats a small portion of the sample, forming a plasma, which as it expands exerts pressure on the sample creating an ultrasonic pulse. Operation in the ablative regime produces a much stronger ultrasound pulse than in the thermoelastic regime, as the expansion is a superposition of ablative and thermoelastic generation [27].

Laser detection of ultrasound requires the use of an interferometer or vibrometer [26], but can often measure the exact out-of-plane surface displacement. With standard interferometers only out-of-plane vibration can be detected. A “knife edge” interferometer is usually required to detect in-plane vibration [28].

Laser ultrasound is ideal for high temperature applications due to the large stand-off distance for generation. The ability of the generator to remain several

meters from the high temperature sample allows for standard equipment to be used in a high temperature environment.

One drawback of laser ultrasound systems is that they are usually much more expensive than a comparable piezoelectric or EMAT system. Additionally, laser ultrasound requires many stringent health and safety regulations due to the risks associated with using a laser powerful enough to generate ultrasound.

1.2.3.3 Piezoelectric Transducers

Piezoelectric transducers are the most commonly used transducer for generating and detecting ultrasound. Commercial piezoelectric transducers are made up of several components, as shown in figure 1.4.

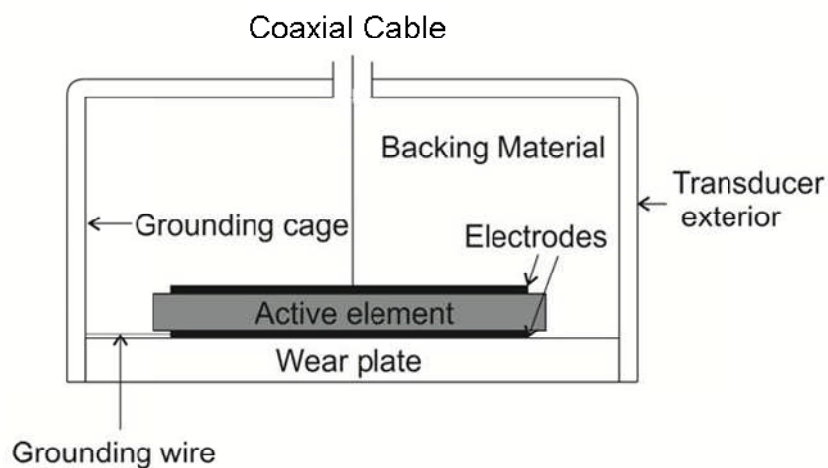


Figure 1.4. A diagram of a commercial piezoelectric transducer with labelled components [17].

The active element is the most important part of the transducer. This is the portion of the transducer that allows it to generate and detect ultrasound and is made of a piezoelectric material (see section 2.2). On the top and bottom of the active element are the electrical contacts used when applying an electric field across the active element.

A large volume of the transducer is made up of the backing material. The primary purpose of this is to damp the active element when the generated pulse has been transmitted, or after a pulse has been received. The wear plate is the part of the transducer placed in contact with the sample to be measured. It may be designed to be hard wearing and to protect the active element from damage that might be incurred due to direct contact with the sample. Additionally, the wear plate should have an acoustic impedance that is as close to the geometric mean of the transducer and the prospective sample as possible [29], to maximise transmission (see section 2.3.4). The grounding cage serves a dual purpose of encasing the transducer, ensuring that the high voltage required for operation is safely isolated and reducing the effect of electromagnetic noise on the transducer. Note that the ground electrode is attached to this, as is the ground from the coaxial cable. In this case the coaxial attachment to the transducer is at the top of the transducer. The exterior of the transducer is usually made of an electrically insulating substance, although if the transducer is properly grounded it can be made from metal [17].

Piezoelectric transducers differ from EMATs or lasers in the need for physical contact and couplant between transducer and sample. This is done to ensure efficient transmission of the ultrasound from the transducer to the sample, as is explained further in section 2.3.4.

The piezoelectric material used in the active element for generating and detecting ultrasound can be in one of two forms. The first is a single crystal, for example a naturally occurring material such as quartz, and consists of a macroscopic crystal structure which arises as a consequence of long range order in the microscopic crystal structure [19, ch 7]. Naturally occurring piezoelectrics were the first to be discovered and characterised [30]. Single crystal materials can be hard to

fabricate, although some, like quartz, are more simple to manufacture [19, ch 7]. Single crystals can also be angle cut to produce different wavemodes.

The second form of piezoelectric elements are ceramic materials, such as lead zirconate titanate (PZT) which are much easier to manufacture than single crystals but have their own drawbacks. PZT is the most commonly used piezoelectric material for ultrasound transducers, but it performs poorly at high temperatures, with a Curie temperature of only 350°C [7], and its lead content makes it environmentally unfriendly. Ceramics are generally less piezoelectrically active than single crystals [2], as their domains are not uniformly oriented, and also require polarisation [1], explained further in section 4.3, in order to be made active. These drawbacks are mitigated by the versatility in the shapes and sizes in which ceramics can be fabricated, as well as their methods of production. Additionally the active direction of a ceramic piezoelectric is chosen when it is polarised, as opposed to single crystals which must be cut and prepared along the crystal axes in order to be effective in the correct direction [31].

There are many different types of piezoelectric materials, with PZT being the most widely used for NDT, although there are few suitable for high temperature use. Specific high temperature piezoelectrics include bismuth titanate ($\text{Bi}_4\text{Ti}_3\text{O}_{12}$), lithium niobate (LiNbO_3) and aluminium nitride (AlN) [32]. The reason that these materials are specifically mentioned as high temperature transducers is due to their high Curie temperature (T_c), which is the temperature at which a material is no longer piezoelectric, and this is discussed in section 2.2.

A number of piezoelectric materials and their Curie temperatures are detailed below:

Material	Curie Temperature [32]
Lead Zirconate Titanate	350°C
Bismuth Titanate	670°C
Lithium Niobate	1210°C
Aluminium Nitride	None known

Table 1. The Curie temperatures of several high temperature piezoelectric materials, using lead zirconate titanate as a comparison of the limits of more widely used transducers.

As can be seen in table 1, bismuth titanate has a relatively low Curie temperature when compared to lithium niobate and aluminium nitride. However, it is simpler to fabricate and more chemically stable and is still suitable for use in the petrochemical and power generation industries. Further motivation for the use of bismuth titanate in this project is due to its relative ease of production and lack of other drawbacks. Lithium niobate loses oxygen from its crystal structure at temperatures above 800°C [33], well below its T_c , causing the destruction of the transducer. While aluminium nitride has no known Curie temperature it is extremely difficult to manufacture, as it is only piezoelectric in very thin film form [32]. It also has similar problems to lithium niobate, notably oxidation at temperatures of approximately 700°C [34]. The most common method of manufacture for these films is chemical vapour deposition [8], a very expensive and difficult method of manufacture.

One drawback of piezoelectrically generated ultrasound is that, excluding immersion testing, it is a direct contact method, meaning that the operating temperature of the transducer will be the same as the temperature of the sample being inspected. Working at this high temperature produces its own difficulties with couplants, namely finding one that remains in the correct form across the entire operating range to conduct the ultrasound from the transducer to the sample.

Other lower temperature piezoelectrics can be adapted to high temperature operation by using active cooling or baffle rods [35]. Both of these steps decrease the temperature of the active element of the transducer. Active cooling is a simple process that uses a substance, usually air or water, to carry heat away from the transducer. Baffle rods can be attached to transducers to increase their separation from the hot sample under investigation, to allow the element to remain cool. These methods allow the transducer to continue operating in environments above the T_c of the active element of the transducer.

References

1. "Piezoelectric thick bismuth titanate/lead zirconate titanate composite film transducers for smart NDE of metals" Kobayashi, M., Jen, G., *Smart Materials & Structures* **13**, Issue 4, 2004, Pages 951-956
2. "Enhanced piezoelectric properties of lead zirconate titanate sol-gel derived ceramics using single crystal $PbZr_{0.52}Ti_{0.48}O_3$ cubes" Lin, Y.R., Andrews, C., Sodano, H.A., *Journal Of Applied Physics* **108**, Issue 6, 2010, Pages 1-6
3. "Combined laser spot imaging thermography and ultrasonic measurements for crack detection" Burrowsm, S.E., Rashed, A., Almond, D.P., Dixon, S., *Nondestructive Testing and Evaluation* **22**, 2007, Pages 217-227

4. "Ultrasonic arrays for monitoring cracks in industrial plant at high temperatures"
Kirk, K.J., McNab, A., Cochran, A., Hall, I.D., Hayward, G., IEEE Transactions on Ultrasonics, Ferroelectrics, and Frequency **46**, 1999, Pages 311-319
5. "Electromagnetic acoustic transducers for testing power station boiler tubes"
Dixon, S., Edwards, C., Palmer, S.B., Crowther, P., Review of Progress in QNDE **18B**, 1999
6. "An Evaluation of Emat Technology for High-Temperature NDE" Light, G.M., Demo, J., NDTnet **3**, 1998
7. "High temperature ultrasonic transducers for imaging and measurements in a liquid Pb/Bi eutectic alloy" Kazys, R., Voleisis, A., Sliteris, L., et al. IEE Transactions On Ultrasonics Ferroelectrics And Frequency Control **52**, Issue 4, 2005, Pages 525-537
8. "High-Frequency, High-Temperature Ultrasonic Transducers" Patel, N.D., Nicholson, P.S., NDT International **23**, Issue 5, 1990, Pages 262-266
9. "Initial tests for designing a high temperature EMAT with pulsed electromagnet"
Hernandez-Valle, F., Dixon, S., NDT & E International **43**, Issue 2, 2010, Pages 171-175
10. "High temperature ultrasonic measurements of plant and components for defect detection and monitoring" Dixon, S., Kirk, K.J., Holland, D., Placido, F., Edwards, R., EPSRC Grant EP/G042284/1
11. "Nondestructive Testing Handbook: Infrared and Thermal Testing" Moore, P.O., 2001, American Society for Nondestructive Testing.
12. "Introduction to NDT by Active Infrared Thermography" Maldague, X., Materials Evaluation **60**, Issue 9, 2002, Pages 1-22

13. Manufacturers Specification for FLIR SC655 camera, <http://www.flir.com/thermography/eurasia/en/content/?id=30716> Retrieved 11/04/11
14. "Introduction to Electromagnetic Nondestructive Testing Methods" Libby, H.L., 1971 Wiley Interscience
15. "Review of advances in quantitative eddy current nondestructive evaluation" Auld, B.A., Moulder, J.C., Journal of Nondestructive Evaluation **18**, Issue 1, 1999, Pages 3-36
16. "Electromagnetic Methods of Nondestructive Testing" Lord, W., 1985 Gordon and Breach
17. "Ultrasonic methods of non-destructive testing" Blitz, J., Simpson, G., 1996 University Press, Cambridge
18. "Estimation of the thickness of thin metal sheet using laser generated ultrasound" Dewhurst, R.J., Edwards, C., McKie, A.D.W., Palmer, S.B., Applied Physics Letters **51**, 1987, Pages 1066-1068
19. "Ultrasonic instruments and Devices" Papadakis, E., 1999, Academic Press
20. "EMATS for Science and Industry" Hirao, M., Ogi, H., 2003, Kluwer Academic Publishers
21. "Recent developments using Electromagnetic Acoustic Transducers" Dixon, S., Edwards, C., Palmer, S.B., Insight **44**, 2002, Pages 274-278
22. "Industrially Viable Non-Contact Ultrasound" Palmer, S.B., Dixon, S., Insight **45**, 2003, Pages 211-217
23. "Modelling of Electromagnetic Acoustic Transducers Operating on Ferromagnetic Materials" Ribichini, R., Cegla, F., Nagy, P.B., Cawley, P., Edited by Thompson, D.O., Chimenti, D.E., 36th Annual Review of Progress in Quantitative Nondestructive Evaluation, 2010, Pages 964-971

24. "Effect on ultrasonic generation of a backplate in electromagnetic acoustic transducers" Jian, X., Dixon, S., Edwards, R., et al., *Journal of Applied Physics* **102**, Issue 2, 2007
25. "High temperature operation of multi-watt, axial-flux, permanent magnets microgenerators" Herrault, F., Arnold, D.P., Zana, I., Galle, P., Allen, M.G., *Sensors Actuators Applied Physics* **148**, 2008, Pages 299–305
26. "Laser ultrasonics : techniques and applications" Scruby, C.B., Drain, L.E., 1990, Adam Hilger, Bristol
27. "TEA-CO₂ Laser Generation of Ultrasound in Nonmetals" Taylor, G.S., Hutchins, D.A., Edwards, C., *Ultrasonics* **28**, Issue 6, 1990, Pages 343-349
28. "A differential fibre-optic sensor for the monitoring of ultrasound" Williams, B.A., Dewhurst, R.J., *Transactions of the Institute of Measurement and Control* **20**, Issue 5, 1998, Pages 243-255
- 29 "Wear plate for piezoelectric ultrasonic transducer arrays" Brisken, A.F., Smith, L.S., United States Patent 4211949
30. "Piezoelectric transducers and applications" Arnau, A., 2008, Springer
31. "Industrial minerals & rocks: commodities, markets, and uses" Kogel, J.E., Trivedi, N.C., Barker, J.M., Krukowsk, S.T., 2006, Society for Mining, Metallurgy, and Exploration
32. "High temperature ultrasonic transducers: review" Kažys, R., Voleišis, A., Voleišienė, B., *Ultragarsas (Ultrasound)* **63**, 2008, Pages 1392-2114
33. "LiNbO₃-based piezoelectric ceramics prepared from sol-gel derived powders" Nibou, L., Manier, M., Mercurio, J.P., *Annales De Chimie-Science Des Materiaux* **23**, 1998, Pages 135-138

34. "Oxidation stages of aluminium nitride thin films obtained by plasma-enhanced chemical vapour deposition (PECVD)" Azema, N., Durand, J., Berjoan, R., Dupuy, C., Cot, L., *Journal of the European Ceramic Society* **8**, Issue 5, 1991, Pages 291-298
35. "300° clamp-on ultrasonic transducers for measuring water flow and level" Lynnworth, L.C., Jossinet, G., Chérifi, E., *Proceedings IEEE Ultrasonic Symposium*, 1996, Pages 407-412

2. Production and Operation of Piezoelectric Transducers

In this chapter the theoretical and practical background to this research will be presented. The focus of this research is the fabrication of high temperature transducers of bismuth titanate ($\text{Bi}_4\text{Ti}_3\text{O}_{12}$) using a sol-gel method. In order to cover the relevant information the chapter will be split into three sections; sol gel theory, the piezoelectric effect and finally the theory behind the proposed ultrasonic testing techniques.

2.1 Sol Gel Techniques

The material being fabricated in this research is bismuth titanate, which is usually fabricated in industry using a milled oxide method, where oxide powders are milled together. Sol gel describes a method of chemical preparation in which a sol transforms into a gel, and is commonly used for preparing ceramic materials, particularly film coatings and extremely fine powders [1].

A sol is a colloidal suspension of a solid in a liquid. Broadly speaking, there are two types of sol; particulate sols, which are a suspension of nano-sized particles in a liquid, and polymeric sols, which are a suspension of branched macromolecules in a liquid. A gel is a two phase compound composed of an interlinking network and a liquid. By weight gels are mostly liquid, although their behaviour is closer to that of a solid [2].

This method has some advantages compared to other methods (such as the milled oxide method) for example, the final product is more homogenous due to the mixing of the precursors in a liquid state, which leads to higher quality ceramic transducers. Additionally, the firing temperatures required to produce the ceramics

are lower than when other methods are used, as the smaller particle size requires less heat to crystallise.

In this project two sols are mixed to form a single gel; a titanium sol and a bismuth sol, both of which are polymeric sols. The process of gelling occurs due to the expansion of the polymer network within the mixed sol [2]. While both metal oxide compounds are known to form polymer networks, it is unknown whether they form two separate homopolymers or a single copolymer. However, it is known that both alkoxides form polymer chains by the process of step polymerisation, which means that multiple smaller chains form individually before crosslinking into larger chains while approaching the final gel state, shown in figure 2.1a.

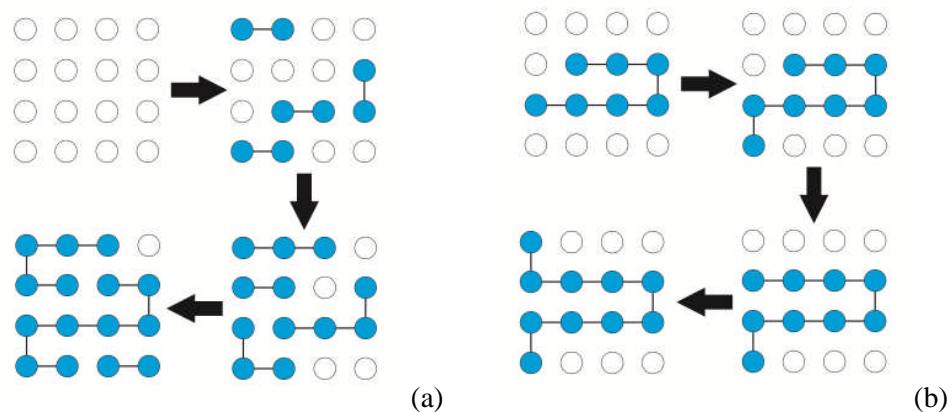


Fig 2.1. Figures showing (a) step polymerisation and (b) chain polymerisation.

These figures show two different processes by which polymer growth occurs.

This is in comparison to chain polymerisation where only a single monomer is added at a time to the chain, as shown in figure 2.1b.

The method of polymer growth in the sols used in this project is by condensation, where two active sites join by the production of a water molecule. Titanium is an atom with four active sites while bismuth has only three. This implies

that there is a significantly higher order of complexity in a titanium homopolymer than exists in a bismuth homopolymer [2].

It should be noted that the titanium and bismuth sols were prepared from stock chemicals of titanium propoxide and bismuth nitrate pentahydrate. Titanium propoxide is a metal alkoxide suitable for the sol gel method, although its gelling rate in air was found to be too rapid to allow sufficient mixing with the bismuth precursor. Bismuth nitrate is a crystal with a very low solubility, being insoluble in water, ethanol and acetone. Additional steps are taken to modify these precursors.

To reduce the reactivity of the titanium propoxide ($Ti(OC_3H_7)_4$) the coordination of the titanium ion is increased by forming a complex with acetate ions through a nucleophilic addition reaction [3];



This is done by the addition of acetic acid to the titanium propoxide in a ratio of 4:1. This stabilises the compound sufficiently for it to be exposed to air without gelling. The structure of this chemical is shown in figure 2.2.

The bismuth nitrate crystals are dissolved in acetylacetone to form another stable complex. Although the nature of the molecule produced is unknown, its exact structure is beyond the scope of the research presented here.

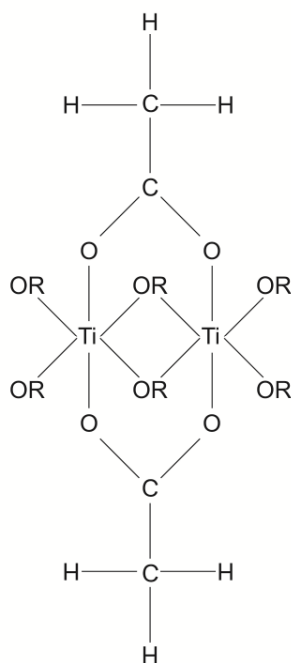
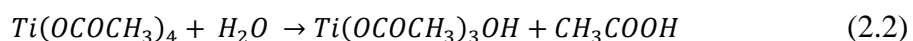


Figure 2.2. The chemical structure of the titanium complex described in equation 2.1, where *R* refers to the alkyl group (OC_3H_7).

Both the sols gel by a process of step polymerisation through condensation. For this to occur, however, an intermediate step of hydrolysis must first occur. This happens when one of the ligands on an active site is replaced by a hydroxyl (OH) ligand. This is shown for titanium acetate in equation 2.2.



These hydrolysis reactions are an intermediate step in the process of polymerisation. After an alkyl group, such as the $(OCOCH_3)$ group above, has been replaced with a hydroxyl group it can interact with another hydroxyl group on a different atom in the process known as condensation.

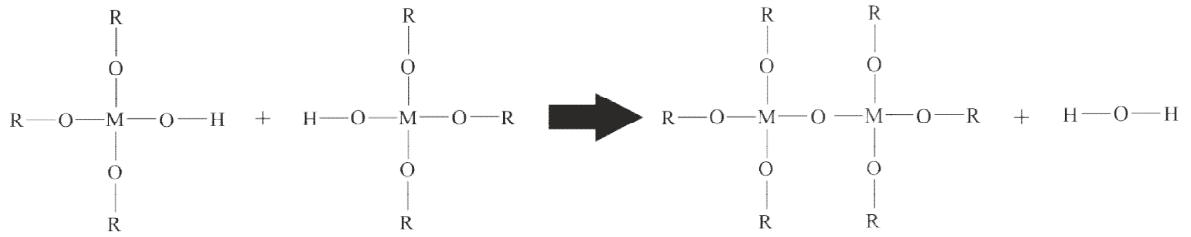


Figure 2.3. The general case of a condensation reaction, where M is a metal ion, R is an alkyl and O and H are oxygen and hydrogen atoms.

This process is shown in figure 2.3 and is the basis by which the polymer chain in this sample grows. It is important to note that, although the general condensation reaction in figure 2.3 occurs between two identical atoms, resulting in the creation of a dimer, a copolymer can be created if the reaction occurs between different atoms. The size of a bismuth atom in comparison with a titanium atom will limit copolymer formation through steric hindrance [4], due to the large charge of the bismuth nucleus, though it will still occur.

2.2 The Piezoelectric Effect

The piezoelectric effect was first demonstrated in 1880 by Pierre and Jacques Curie [5]. They showed that, by applying a stress to certain crystals, an electric potential could be generated. The inverse piezoelectric effect, where by applying an electric potential stress could be induced in a crystal, was also demonstrated by them in 1881, and is shown schematically in figure 2.4.

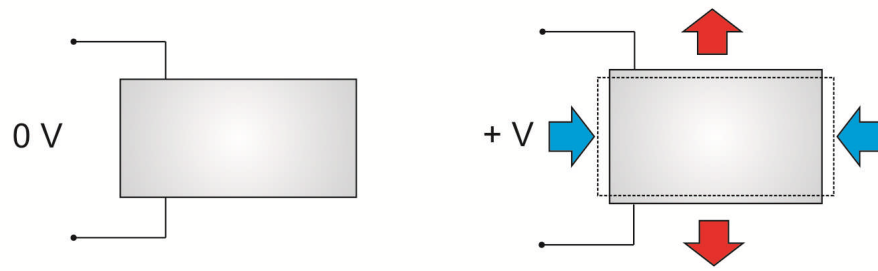


Figure 2.4. The inverse piezoelectric effect; when an electric field is applied to a piezoelectric material stress is induced within the material, causing its shape to change. The scale of the shape change has been exaggerated in this figure. The red arrows represent the expansion resulting from the piezoelectric effect and the blue arrows are the contraction required to maintain the volume of the material.

Figure 2.4 shows the effect of applying an electric field to a piezoelectric crystal. The simple form of the equation governing the direct piezoelectric effect is [6]:

$$P = d\sigma \quad (2.3)$$

where P is the polarisation, d is the piezoelectric modulus and σ is the stress. For the reverse piezoelectric effect it is as follows [6]:

$$\epsilon = dE \quad (2.4)$$

where ϵ is the strain and E is the Electric field. It will be demonstrated later that while these equations are approximately true, a degree of accuracy is lost by treating the quantities involved as scalars rather than tensors.

In many piezoelectric crystals the lack of central symmetry arises in a type of crystal structure called a perovskite. This causes the formation of an electric dipole in

the material. Barium titanate (BaTiO_3) is a commonly used piezoelectric that has a perovskite structure, and this is shown in figure 2.5.

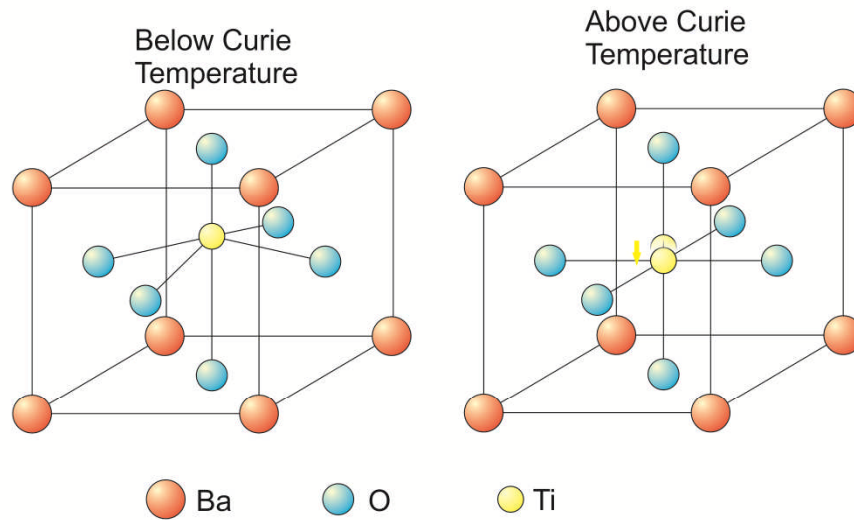


Figure 2.5. The perovskite structure of barium titanate below and above its Curie temperature. Note the asymmetry in the image of the crystal below its Curie temperature. It is this asymmetry that is responsible for the piezoelectric effect.

Below its Curie temperature, T_c , the crystal is tetragonal and contains an electric dipole due to the off-centre position of the unit cell's titanium atom. As the temperature rises to T_c , 120°C [7, p.10], the titanium atom shifts to the centre of the unit cell as the crystal structure becomes cubic, and the asymmetry leading to piezoelectricity is lost.

2.2.1 Tensor Treatment of Piezoelectricity

The analysis of piezoelectricity given by equations 2.3 and 2.4 is a scalar simplification of an effect which should ideally be described using third order tensors. Tensors are a mathematical notation well suited to describing complex physical phenomena. A 0th order tensor is a scalar and a 1st order tensor is a vector. A

2nd order tensor can be represented as a matrix and a 3rd order tensor can be represented as a three dimensional matrix. It is important to note that, while a matrix is a convenient way of representing a second order tensor, a matrix itself is not necessarily a tensor. Equation 2.3 can be rewritten using tensors [6]:

$$P_i = d_{ijk}\sigma_{jk} \quad (2.5)$$

where the stress in a material, σ_{jk} , is now described by a second order tensor containing both shear and axial stress and the polarisation, P_i , is a first order tensor. The subscript i is used to denote a polarisation direction in the crystal, and j and k are used to describe directions in the stress tensor. The piezoelectric modulus that relates them, d_{ijk} , must therefore be a third order tensor. Similarly, the equation for the reverse piezoelectric effect can be rewritten using tensors;

$$\epsilon_{jk} = d_{ijk}E_i \quad (2.6)$$

where ϵ_{jk} is the strain tensor and E_i is the electric field.

A third order tensor, such as d_{ijk} , can be expressed as a set of three matrices;

$$\begin{pmatrix} d_{111} & d_{112} & d_{113} \\ d_{121} & d_{122} & d_{123} \\ d_{131} & d_{132} & d_{133} \end{pmatrix} \quad \begin{pmatrix} d_{211} & d_{212} & d_{213} \\ d_{221} & d_{222} & d_{223} \\ d_{231} & d_{232} & d_{233} \end{pmatrix} \quad \begin{pmatrix} d_{311} & d_{312} & d_{313} \\ d_{321} & d_{322} & d_{323} \\ d_{331} & d_{332} & d_{333} \end{pmatrix} \quad (2.7)$$

This third order tensor has 27 components, although these can be reduced using arguments of symmetry for the strain and stress tensors, σ_{jk} and ϵ_{jk} , making d_{ijk} symmetrical in the j and k indices [8]. The symmetry of d_{ijk} leads to relations such as;

$$d_{112} = d_{121} \quad (2.8)$$

This symmetry in j and k allows the 27 components to be reduced to 18, giving;

$$\begin{pmatrix} d_{111} & d_{112} & d_{113} \\ d_{112} & d_{122} & d_{123} \\ d_{113} & d_{123} & d_{133} \end{pmatrix} \quad \begin{pmatrix} d_{211} & d_{212} & d_{213} \\ d_{212} & d_{222} & d_{223} \\ d_{213} & d_{223} & d_{233} \end{pmatrix} \quad \begin{pmatrix} d_{311} & d_{312} & d_{313} \\ d_{312} & d_{322} & d_{323} \\ d_{313} & d_{323} & d_{333} \end{pmatrix} \quad (2.9)$$

There is a reduced notation, or matrix notation, which is designed to simplify the process of representing the tensors on paper. The relationship between the j and k

suffixes in the full tensor notation and the new suffixes from the matrix notation is shown in table 2.

Tensor notation	11	22	33	23, 32	31, 13	12, 21
Reduced notation	1	2	3	4	5	6

Table 2. The relationship between the j and k indices in tensor notation and the single index used in reduced notation to replace them.

Hence the component d_{112} now relates to d_{16} . This reduced notation is simplified further by defining the following substitution:

$$d_{112} + d_{121} = d_{16} \quad (2.10)$$

and similarly for the other off-diagonal terms. This substitution allows the off-diagonal terms in the matrix to be rewritten using:

$$d_{112} = d_{121} = \frac{1}{2}d_{16} \quad (2.11)$$

giving the following definition of the tensor:

$$\begin{pmatrix} d_{11} & \frac{1}{2}d_{16} & \frac{1}{2}d_{15} \\ \frac{1}{2}d_{16} & d_{12} & \frac{1}{2}d_{14} \\ \frac{1}{2}d_{15} & \frac{1}{2}d_{14} & d_{13} \end{pmatrix} \begin{pmatrix} d_{21} & \frac{1}{2}d_{26} & \frac{1}{2}d_{25} \\ \frac{1}{2}d_{26} & d_{22} & \frac{1}{2}d_{24} \\ \frac{1}{2}d_{25} & \frac{1}{2}d_{24} & d_{23} \end{pmatrix} \begin{pmatrix} d_{31} & \frac{1}{2}d_{36} & \frac{1}{2}d_{35} \\ \frac{1}{2}d_{36} & d_{32} & \frac{1}{2}d_{34} \\ \frac{1}{2}d_{35} & \frac{1}{2}d_{34} & d_{33} \end{pmatrix} \quad (2.12)$$

This tensor can now be rewritten in a single matrix of 18 components in order to simplify its representation on paper:

$$\begin{pmatrix} d_{11} & d_{12} & d_{13} & d_{14} & d_{15} & d_{16} \\ d_{21} & d_{22} & d_{23} & d_{24} & d_{25} & d_{26} \\ d_{31} & d_{32} & d_{33} & d_{34} & d_{35} & d_{36} \end{pmatrix} \quad (2.13)$$

In order to be consistent the tensor σ_{jk} must be rewritten as well;

$$\begin{pmatrix} \sigma_{11} & \sigma_{12} & \sigma_{13} \\ \sigma_{21} & \sigma_{22} & \sigma_{23} \\ \sigma_{31} & \sigma_{32} & \sigma_{33} \end{pmatrix} \rightarrow \begin{pmatrix} \sigma_1 & \sigma_6 & \sigma_5 \\ \sigma_6 & \sigma_2 & \sigma_4 \\ \sigma_5 & \sigma_4 & \sigma_3 \end{pmatrix} \quad (2.14)$$

Equation 2.5 can now be rewritten to take advantage of this reduced notation:

$$P_i = d_{ij}\sigma_j \quad (2.15)$$

The inverse piezoelectric effect (equation 2.6) can also be written using matrix notation. However, it requires that ϵ_{jk} be rewritten in a similar way to d_{ijk} . Looking at a single portion of the tensor, ϵ_{12} :

$$\epsilon_{12} = \sum_{i=1}^3 d_{i12}E_i \quad (2.16)$$

which, using the new notation becomes:

$$\epsilon_{12} = \frac{1}{2}d_{16}E_1 + \frac{1}{2}d_{26}E_2 + \frac{1}{2}d_{36}E_3 \quad (2.17)$$

To write equation 2.17 fully in reduced notation ϵ_{12} is defined:

$$\epsilon_{12} = \epsilon_{21} = \frac{1}{2}\epsilon_6 \quad (2.18)$$

with ϵ_{jk} rewritten as:

$$\begin{pmatrix} \epsilon_{11} & \epsilon_{12} & \epsilon_{13} \\ \epsilon_{21} & \epsilon_{22} & \epsilon_{23} \\ \epsilon_{31} & \epsilon_{32} & \epsilon_{33} \end{pmatrix} \rightarrow \begin{pmatrix} \epsilon_1 & \frac{1}{2}\epsilon_6 & \frac{1}{2}\epsilon_5 \\ \frac{1}{2}\epsilon_6 & \epsilon_2 & \frac{1}{2}\epsilon_4 \\ \frac{1}{2}\epsilon_5 & \frac{1}{2}\epsilon_4 & \epsilon_3 \end{pmatrix} \quad (2.19)$$

This allows equation 2.6 to be rewritten in matrix notation:

$$\epsilon_j = d_{ij}E_i \quad (2.20)$$

This step is a standard step taken in many published works considering piezoelectricity [9], with the most notable example of the use of reduced notation being that of the value d_{33} . This is widely used as a measure of the effectiveness of a longitudinal wave ultrasound transducer. The corresponding value in tensor notation is the d_{333} value, which is a measure of the deformation of a piezoelectric material in an axial direction corresponding to the electric response in that same axial direction.

2.2.2 Piezoelectric Effect in Bismuth Titanate

Piezoelectricity in bismuth titanate is due to a triple pseudo-perovskite formation known as an Aurivillius structure [10]. This has three sub-structures which approximate to perovskite structures and is shown in figure 2.6.

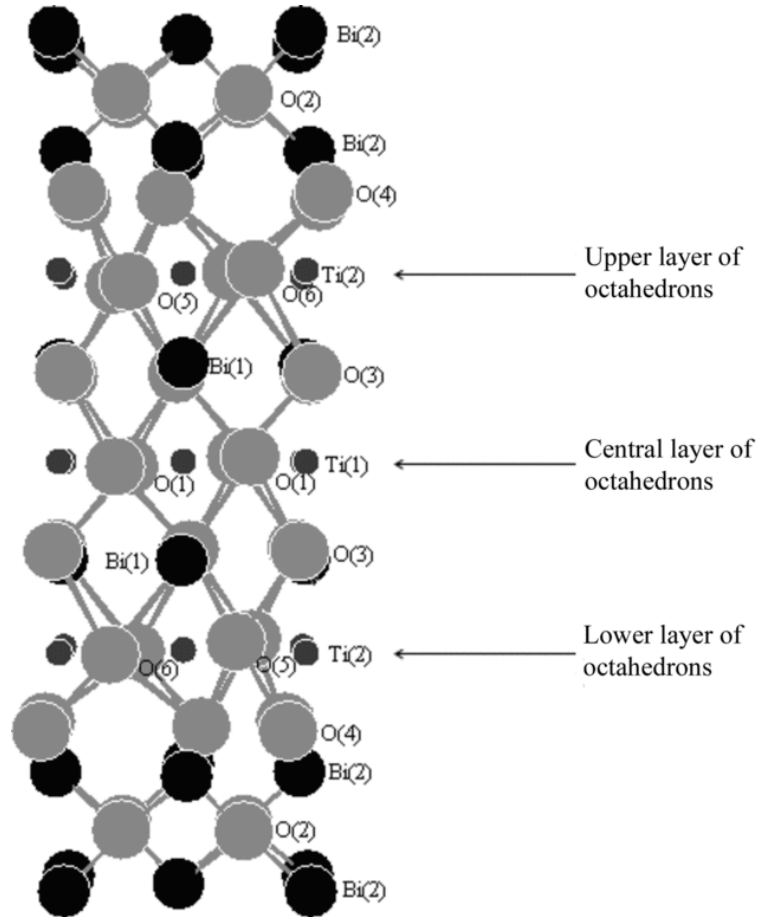


Figure 2.6. Structure of bismuth titanate, image taken from reference [10].

These sub structures will each produce a piezoelectric response, and, although two of the structures are at an angle to the crystal axis, their lateral responses should cancel each other out. These pseudo-perovskites exist along the b axis of the crystal and as the crystal approaches T_c the asymmetry is lost, as this axis changes to become the same length as the a axis, changing the crystal structure to tetragonal [10].

Bismuth titanate also exhibits ferroelectricity. This describes a material that produces a spontaneous and reversible electric polarisation when an external electric field is applied to it [11]. This is in direct analogy to the magnetic polarisation of ferromagnetic materials, and is where the phenomenon received its name (most ferroelectrics do not contain iron in their structure). Like a ferromagnetic material, a ferroelectric material will show a distinct hysteresis when a reversing electric field is applied to it. The ability of the three dipoles in bismuth titanate to be reversed by the application of an electric field make it a ferroelectric.

In conjunction with its piezoelectric and ferroelectric behaviour, bismuth titanate is also pyroelectric [12]. This means that when the crystal is heated an electric field will be produced within the crystal. If there is a temperature gradient across a pyroelectric material there will also be a voltage gradient. However, for reasonably constant temperatures this will simply manifest as a DC offset in the measured voltage signal. The equation for pyroelectricity is [6];

$$\delta P_i = p_i \delta T \quad (2.21)$$

where P_i is the spontaneous polarisation vector, p_i is the coefficient of pyroelectricity and T is temperature. The subscript i indicates the direction of the effect, which must be considered in anisotropic crystals.

2.3 Ultrasound Propagation

Ultrasound is, simply, the propagation of vibrations with a frequency greater than 20 kHz through media. These vibrations travel through the medium via interactions between the basic particles that form the medium. As each particle vibrates it passes the vibrations on to its neighbouring particles, which in turn pass the vibrations to their neighbouring particles, and thus ultrasound propagates through

the medium [13]. The transducers in this research will be used to perform pulse-echo measurements, described in section 2.3.5.

2.3.1 Ultrasonic Transducers

The most common type of transducers for NDT are piezoelectric transducers, as discussed in section 1.2.3.3, where ultrasound is generated through oscillation of the piezoelectric element. Transducers generally have a resonant frequency at which they are most efficient at producing ultrasound [14]. This is due to the formation of standing waves inside the transducer [15], as shown in figure 2.7.

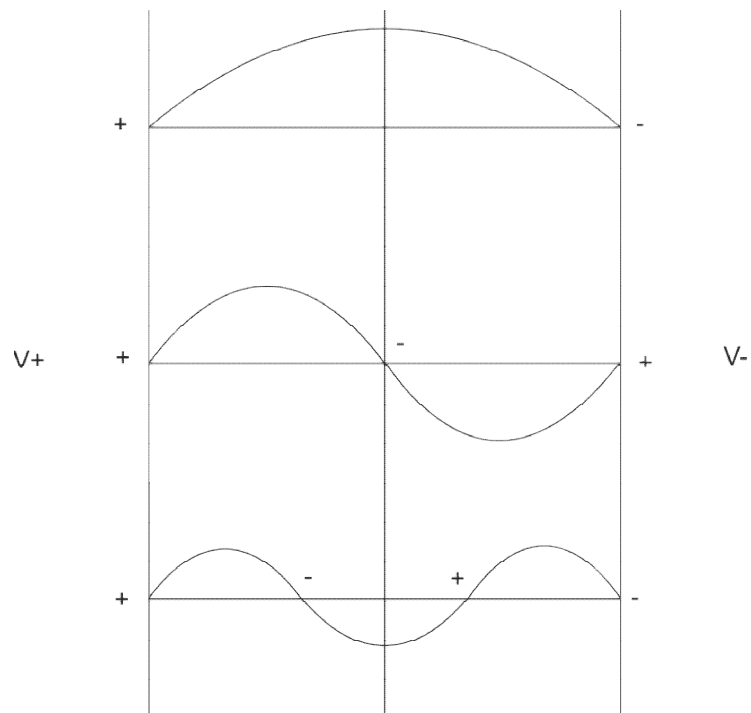


Figure 2.7. Harmonics in a piezoelectric transducer. The second harmonic wave will not form as it would require both sides of the transducer to be at the same voltage.

The resonant frequency of the transducer is the fundamental mode of the standing wave within it [15]. The transducer will also have higher harmonics which

will also produce ultrasound efficiently; however, as can be seen in figure 2.7, only the odd harmonics can satisfy the boundary condition that opposite sides of the transducer must be at different voltages.

2.3.2 Ultrasonic waves

There are two main types of ultrasonic wave; surface waves and bulk waves. As their name suggests bulk waves propagate within a sample, while surface waves propagate on the exterior of the sample. Surface waves are actually a superposition of bulk waves that satisfy the boundary conditions present when propagating at the surface.

Bulk waves are subdivided into two types of wave motion; shear and longitudinal. Longitudinal waves propagate in the same direction as the motion of the particles that make up the wave, with the best known example being that of sound waves in air.

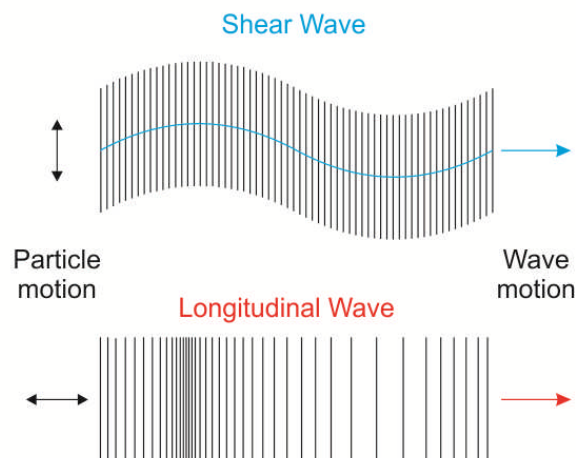


Figure 2.8. The propagation of longitudinal and shear waves and their particle motion.

Shear waves propagate perpendicular to the particle motion of the wave, and are also known as transverse waves. In solid media both shear and longitudinal waves are common, but shear waves will only propagate in the most viscous of fluids [13]. This is due to the ability of fluids to move freely when subjected to pressure, forming compression waves in preference to shear waves [13].

One of the surface waves used in NDT is a Rayleigh wave. This type of wave propagates with an elliptical particle motion, and has a mix of both longitudinal and shear type propagation [13]. Figure 2.9 shows a diagram of the particle motion and propagation. Although Rayleigh waves are a surface wave, there is some penetration into the bulk of a sample. This penetration is dependent on the frequency of the wave, with the amplitude of the wave falling away exponentially as the depth of penetration increases. The majority of the wave energy is within one wavelength of the sample surface.

Rayleigh Wave

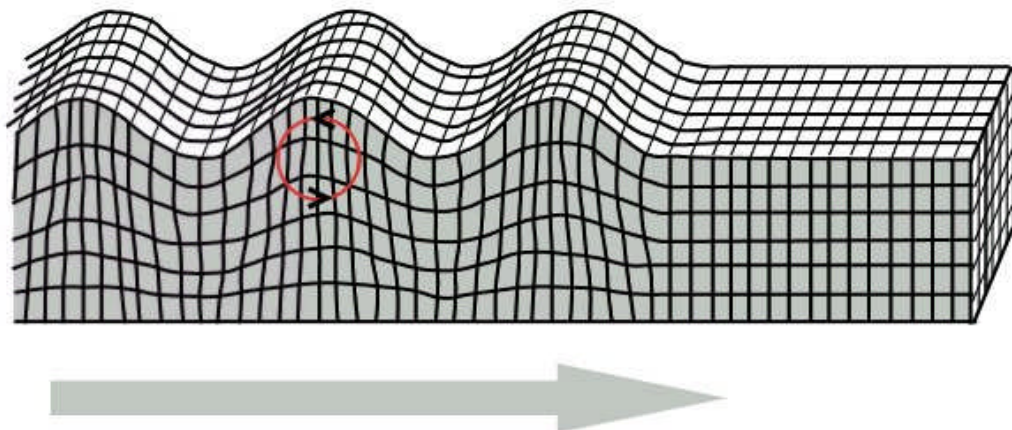


Figure 2.9. The propagation of a Rayleigh wave and its particle motion taken from [16].

For plates whose thickness is comparable to, or less than, the wavelength of the wave, the surface wave exists as a Lamb wave [13]. Lamb waves have two modes of propagation; symmetric and anti-symmetric, as shown in figure 2.10. The particle motion in Lamb waves is again elliptical [17].

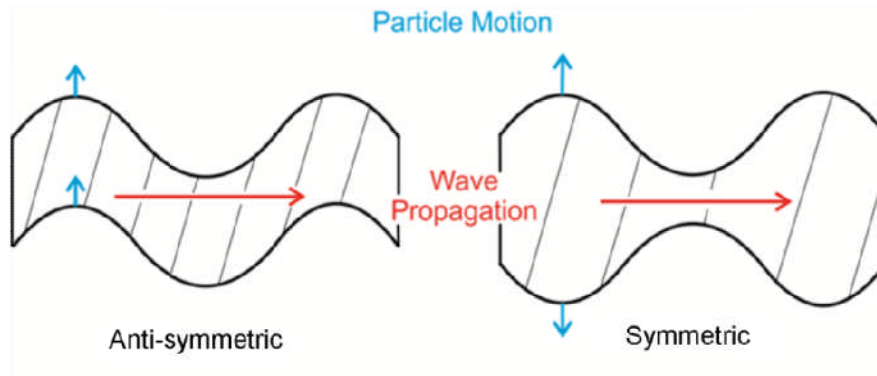


Figure 2.10. The wave propagation and particle motion of symmetric and anti-symmetric Lamb waves

2.3.3 Attenuation of Bulk Waves

Ultrasound will not travel indefinitely in a medium, and as the wave propagates it loses energy as it spreads out in the bulk and due to damping and scattering [13]. Most solid metals are crystalline in structure, although they seldom have long range order [5, ch.7]. The structure is usually made up of smaller crystalline structures known as grains. In addition to transmission losses, explained further in section 2.3.4, there is also friction produced in the dislocations between grains as they vibrate [18]. A further source of attenuation is the existence of microscopic cracks between grains, causing voids through which the ultrasound may be unable to pass. Attenuation due to the grain structure is known as Rayleigh scattering [13], with an attenuation coefficient α given by:

$$\alpha = \frac{kD^3}{\lambda^4} \quad (2.22)$$

where k is a measure of the anisotropy of the system (adjusts the mean linear dimension based on the anisotropy of the granular structure), D is the mean linear dimension of the grains and λ is the wavelength of the ultrasound [13].

2.3.4 Transmission of Ultrasound between Media

One of the key considerations in ultrasound propagation is the transmission of ultrasound between two media. When an ultrasonic wave strikes an interface a portion of the wave will be reflected and a portion will be transmitted. If the wave is incident on the surface at an angle, instead of orthogonal to it, a portion of the wave may also be mode converted into a different type of wave [13, p24]. The equation governing the propagation of ultrasound across an interface is as shown;

$$\alpha_r + \alpha_t \leq 1 \quad (2.23)$$

where α_r is the coefficient of reflection, α_t is the coefficient of transmission and the less than or equal to one accounts for both loss and mode conversion at the interface. These are further defined in relation to the characteristic impedances [13] of media 1 and 2:

$$\alpha_r = \frac{(Z_2 - Z_1)^2}{(Z_2 + Z_1)^2} \quad (2.24)$$

where Z_1 is the characteristic impedance of the first medium and Z_2 is the characteristic impedance of the second medium, and

$$Z_\alpha = c_\alpha \rho_\alpha \quad (2.25)$$

where c_α is the speed of sound in the medium and ρ_α is its density. For transmission with no loss using equations 2.23 and 2.24 it can be shown that:

$$\alpha_t = \frac{4Z_1Z_2}{(Z_1 + Z_2)^2} \quad (2.26)$$

The coefficient of transmission is a measure of the efficiency of a boundary in allowing ultrasound to propagate across it. Coupling is a term often used to describe the transmission efficiency of an interface between media [13, p.21].

In order to maximise the usefulness of a transducer the coupling between it and the sample medium must be as high as possible. When a transducer is placed on a sample the microscopic picture of their boundary can be starkly different to what is observed by the human eye, as shown in figure 2.11.

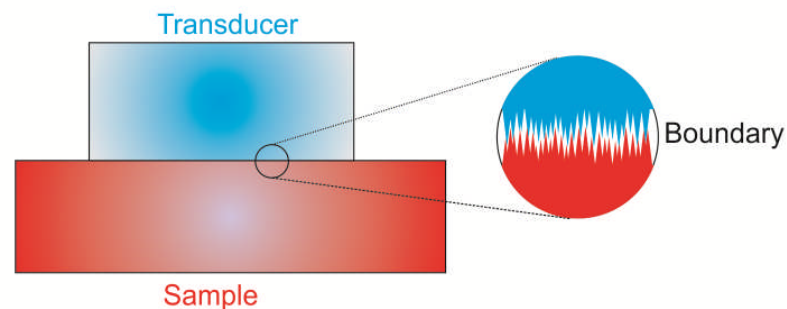


Figure 2.11. Image showing roughness at microscopic level at a boundary between two media.

The apparently close bond between transducer and sample is seldom smooth. Many miniscule pockets of air can exist between the two, causing poor coupling. In many situations this is overcome with the use of couplants; materials designed to fill the gaps between transducer and sample and to provide much better transmission of sound through better coupling. This occurs because the characteristic impedance of the couplant is much closer to both the sample and transducer than the air is. Often, for boundaries between media with vastly different impedances, a medium of intermediate impedance is used, and the process is known as impedance matching

[19]. At high temperatures the couplants used have a very short operational lifespan [20], leading to the suggestion of alternative solutions, such as thick film transducers bonded to the sample.

The use of thick films, as described later, can eliminate the need for couplants by filling the microscopic gaps when the transducer is grown directly onto the sample [20]. This allows inspections to be carried out “dry”, without couplant. This is highly desirable in high temperature ultrasound due to the scarcity of materials capable of acting as couplants beyond 200°C [20].

2.3.5 Using Ultrasound for Thickness Testing

The uses of ultrasound in NDT are varied, but one common use is in thickness gauging [13, ch.6.3]. This quantitatively examines the thickness of a sample, allowing effects like corrosion to be monitored. It can also provide quality assurance in industrial processes such as the manufacturing of metal billets or pipe. It is usually performed with one transducer and relies on using the arrival time of a reflected ultrasound pulse to work out the thickness of the sample, using equation 2.27.

$$2h = ct \tag{2.27}$$

where h is the thickness of the sample, c is the velocity of the ultrasound in the medium and t is the time taken for the ultrasound to travel the path shown in figure 2.12. Although the standard technique usually only examines the arrival time of the first reflected pulse, enhanced accuracy can be obtained in less attenuating samples by averaging the time taken for multiple echoes to travel along the path.

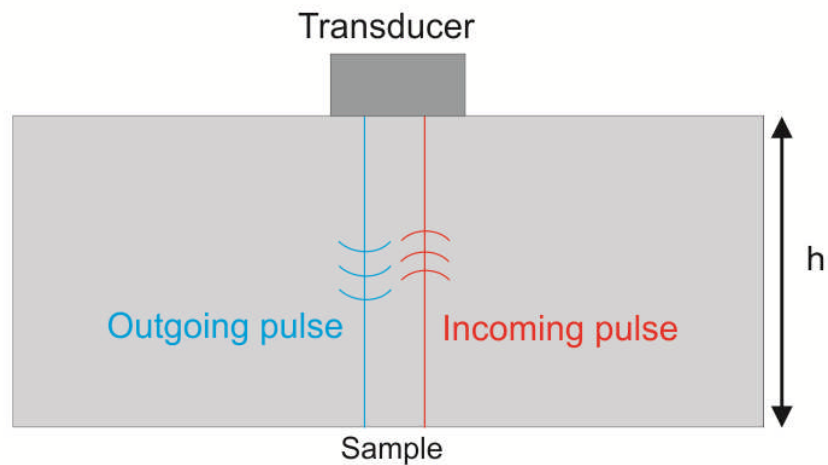


Figure 2.12. Setup for thickness gauging using pulse-echo method.

Another use of ultrasound is in the detection and sizing of flaws and defects. Ultrasonic detection of flaws in the bulk can often be performed using a single transducer setup. In this setup the single transducer acts as both transmitter and receiver, sending ultrasound into the sample and detecting the ultrasound reflected from any defects, as shown in figure 2.13 [13].

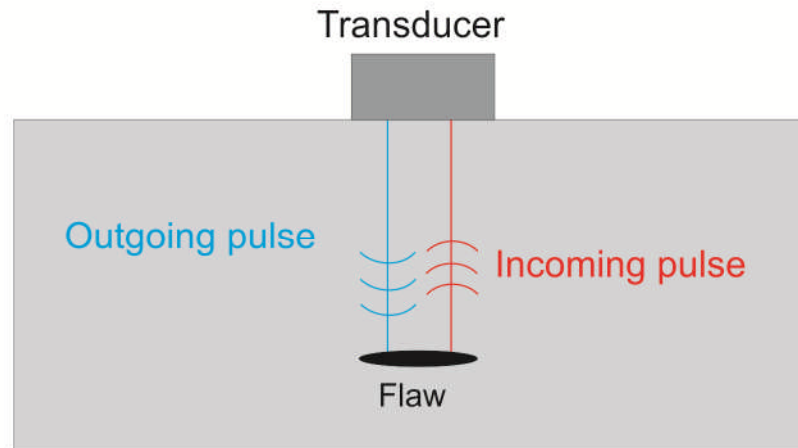


Figure 2.13. Ultrasonic flaw detection, which uses a similar setup to thickness measurements. A flaw can be identified by the presence of an echo arriving before that of the back wall.

Detection of defects can be done in a similar way to thickness gauging, where reflections received by the transducer before the first backwall echo are attributed to flaws, which can then be positioned using the time delay of the echo and the speed of sound in the sample. The lateral dimensions of the defect can be determined by moving the probe and denoting the location where the defect reflection first appears. However, this assumes that the ultrasound beam is the same size as the transducer at all depths, which is often untrue [21]. With a transducer of known beamshape a correction can be applied based on the defect depth. The method also assumes that the transducer is smaller than the defect to be sized, an assumption not present in the 6 dB drop method, which sizes the edge of the flaw at the point where the reflected signal is half what it was in the centre of the flaw [13, ch.8.2.1].

References

1. "Sol-Gel Materials: Chemistry and Applications" Wright, J.D., Sommerdijk, N.A.J.M., 2000, CRC Press
2. "Sol gel science" Brinker, C.J., Scherer, G.W., 1990, Academic Press
3. "Sol-Gel Chemistry" Livage, J., Sanchez, C., Journal of Non-Crystalline Solids **145**, 1992, Pages 11-19
4. "Polymeric Stabilization of Colloidal Dispersions (Colloid Science)" Napper, D.H., 1983, Academic Press
5. "Ultrasonic instruments and Devices" Papadakis, E., 1999, Academic Press
6. "Physical Properties of Crystals" Nye, J.F., 1964, University Press, Oxford
7. "Introduction to ferroic materials" Wadhawan, V.K., 2000, CRC Press
8. "Ferroelectric, dielectric and piezoelectric properties of ferroelectric thin films and ceramics" Damjanovic, D., Reports on Progress in Physics **61**, 1998, Pages 1267–1324
9. "Grain-oriented fabrication of bismuth titanate ceramics and its electrical-properties" Seth V.K., Schulze W.A., IEEE Transactions on Ultrasonics Ferroelectrics And Frequency Control **36**, Issue 1, 1989, Pages 41-49
10. "Phase stability in ferroelectric bismuth titanate: a first-principles study" Shrinagar, A., Garg, A., Prasad, R., Auluck, S., Acta Crystallographica A **64**, 2008, Pages 368-375
11. "Solid State Physics: Advances in Research and Applications, Vol. 4" Chapter 1, Seitz, F., Turnbull, D., 1957, Academic Press
12. "Bismuth titanate from coprecipitated stoichiometric hydroxide precursors" Umabala, A.M., Suresh, M., Prasadarao, A.V., Materials Letters **44**, 2000, Pages 175-180

13. "Ultrasonic methods of non-destructive testing" Blitz, J., Simpson, G., 1996 University Press, Cambridge
- 14 "Experimental Broadband Ultrasonic Transducers Using PVF₂ Piezoelectric Film" Bui, L., Shaw, H.J., Zitelli, L.T., Electronics Letters **12**, 1976, Pages 393-394
- 15 "Nondestructive Evaluation: Theory, Techniques, and Applications" Shull, P.J., 2002, CRC Press
16. United States Geological Survey, Website Accessed 13/04/2011 <http://earthquake.usgs.gov/learn/glossary/?term=Rayleigh%20wave>
17. "Ultrasonic Waves in Solid Media" Rose, J.L., 2004, Cambridge University Press
18. "Non-linear effects of high-power ultrasonics in crystalline solids" Green, R.E., Ultrasonics **13**, 1975, Pages 117-127
19. "Acoustic impedance matching of medical ultrasound transducers" Persson, H.W., Hertz, C.H., Ultrasonics **23**, 1985, Pages 83-89
20. "High temperature ultrasonic transducers: review" Kažys, R., Voleišis, A., Voleišienė, B., Ultragarsas (Ultrasound) **63**, 2008, Pages 1392-2114
21. "Ultrasonic arrays for non-destructive evaluation: A review" Drinkwater, B.W., Wilcox, P.D., NDT&E International **39**, 2006, Pages 525-541

3. Material Characterisation Techniques

In the course of the research one of the key results to achieve was to characterise the materials which were fabricated, both to validate the fabrication techniques and to assess the quality of the fabricated materials. In this chapter the processes by which the bismuth titanate samples were characterised, thermally and crystallographically, will be explained.

3.1 Thermal Characterisation

Thermal characterisation shows the thermal response of a sample to variation in temperature. Several samples of bismuth titanate were examined using a combined differential scanning calorimetry and thermogravimetric analysis (DSC/TGA) setup. This involves the measurement of a sample's weight and the heatflow into it as the sample is heated [1]. These measurements are then compared to an empty crucible in order to eliminate effects such as airflow under the sample lightening the weight measurement, or the heatflow into the crucible interfering with the measurement of the sample.

The sample is placed into a platinum-rhodium crucible and weighed to provide an initial reading for the scales of the machine. The machine then heats the sample continuously to temperatures of up to 1200°C and outputs the heatflow and weight data to a computer.

The heatflow measurements allow the temperature at which changes occur in the sample, such as a glass transition or crystallisation, to be identified. The weight change allows points where samples have undergone certain chemical changes, like

oxidation, to be identified; in an oxidation reaction the sample reacts with oxygen in the atmosphere, and this will increase the weight of the sample.

The profile of the heatflow data can allow for precise identification of the types of transitions taking place in the sample. Exothermic (where heat is given out by the sample) and endothermic (where heat is absorbed by the sample) changes are easy to differentiate, as they are represented by dips and spikes in the data respectively. In addition to the orientation of the peak, its profile will give additional information about the transition occurring. A crystallisation transition can be identified by a typically sharp exothermic peak, when compared to the broader exotherm typical of a glass transition.

In these experiments the samples, weighing between 30mg and 60mg, were heated to 900°C at a rate of 10°C per minute in a combined DSC/TGA machine.

3.2 Crystallographic Characterisation

X-ray diffraction is a technique which examines the crystal structure of materials by using x-rays of wavelength comparable to the lattice spacing of the material. The random orientation of the crystals in a powder sample ensures that all crystal positions are represented evenly. The lattice spacing of the crystal acts as a diffraction grating, providing constructive interference at given angles. The values of these angles allows the size and shape of the crystal lattice to be identified [2]. This allows the purity of the samples to be assessed. In the x-ray diffractometer used here the k_{α} emission peak of copper is used [3]. The monochromatic light, at 0.154 nm, produces peaks in the pattern which are sharp and well defined. The sample is placed in the centre of a beam of x-rays and a detector records the diffraction pattern. The

sample itself is rotated in the diffractometer as the detector moves around it in order to produce a scan, as shown in figure 1.

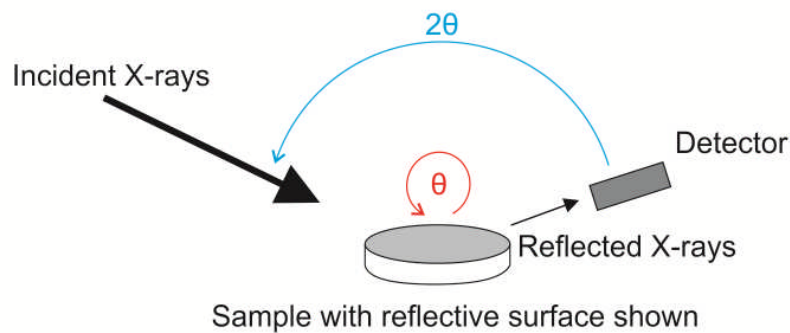


Figure 3.1 The arrangement of sample and its motion through θ , and the detector and its motion through 2θ .

The detector on the powder diffractometer is a 255 channel CCD detector spread over an angle of 3.347° [4]. Each individual element of the detector moves through the 2θ angle and their counts are summed to produce the total count for that angle. The sample was prepared as a pellet, but ground into a powder and packed into a holder, typically containing a few grams of powder.

In addition to the room temperature experiments, several characterisations took place at high temperatures. This is performed by attaching an Anton Paar furnace and sample stage to the diffractometer. The sample is heated by the furnace, allowed to stabilise at a given temperature, then a diffraction pattern is obtained as it would be for a room temperature measurement. This results in a series of diffraction patterns, each obtained at different temperatures. The maximum temperature the furnace can operate at is 1200°C , though that was not reached in this research [5].

The samples for the high temperature experiments were prepared in a similar manner to those for the low temperature experiments, although the sample holder

was smaller to reduce the size of the furnace. Several high temperature experiments were performed, with different temperature steps, equalisation times and scan lengths. The smallest temperature difference between steps was only 1°C, while the largest was 100°C. The time allowed for the sample to reach thermal equilibrium varied similarly, with the shortest being only 5 minutes, while the longest was one hour.

References

1. DSC/TGA 1, Manufactured by Mettler Toledo, Manufacturer's Website, Accessed 19/04/2011
http://uk.mt.com/gb/en/home/products/Laboratory_Analytics_Browse/TA_Family_Browse/TA_Modules_Browse/TGA_Module_TGA_DSC1.html
2. "A profile refinement method for nuclear and magnetic structures" Rietveld, H. M., Journal of Applied Crystallography **2**, 1969, Pages 65–71
3. PANalytical X'pert Pro MPD Specification, Manufacturer's Website, Accessed 12/04/2011 <http://www.panalytical.com/index.cfm?pid=321>
4. PANalytical PIXcel Specification, Manufacturer's Website, Accessed 12/04/2011
<http://www.panalytical.com/index.cfm?pid=1089>
5. Anton Paar High-Temperature Oven-Chamber: HTK 1200N Specification, Accessed 12/04/2011 http://www.anton-paar.com/High-Temperature-Oven-Chamber-HTK-1200N/X-ray-Structure-Analysis-XRD/60_UK_en?product_id=278#Specifications

4. Experimental Techniques Developed for Preparing Bismuth Titanate Transducers

In addition to the standard experimental techniques detailed in the previous chapters, this project explored several novel techniques in sample preparation. Additionally, a novel technique to induce electrical polarisation was also investigated. These new techniques are described in detail, as are several more standard techniques.

4.1 Sample preparation.

Several novel methods of sol-gel preparation of bismuth titanate were developed during the research, although all had common aspects. None of the methods used prefabricated bismuth titanate powder as a precursor [1]. Four slightly different preparations were made, coded for the chemical precursors titanium propoxide (TiP), bismuth nitrate (BiN) and solvents used to prepare the bismuth nitrate;

- acetic acid (CH_3COOH)
- nitric acid (HNO_3)
- nitric acid with water added later in the process (HNO_3 Hydrated)
- acetylacetone (Acac).

The progression in the methods was the result of attempts to improve the quality of the final sample and to reduce the use of hazardous chemicals.

4.1.1 First preparation; TiP/BiN CH₃COOH

The first step in the fabrication of the bismuth titanate piezoelectric transducer was the production of a homogenous powder which could be fired to produce a bismuth titanate ceramic. The first attempt at making such a powder followed a non-standard method developed by altering a method from the literature to utilise available chemicals and used the common precursors of titanium propoxide and bismuth nitrate [2]. These precursors were chosen due to their use in similar research and relatively low cost. The titanium propoxide was decanted into a conical flask and then sealed using a suba-seal in a dry nitrogen glovebox. After being removed from the glovebox, glacial acetic acid was added to the titanium propoxide in the molar ratio of 4:1 using a syringe and hypodermic needle. This created a titanium complex, $Ti_2(OC_3H_7)_4(OCOCH_3)_2$, a more stable chemical which could be used outside of a dry nitrogen atmosphere.

The bismuth nitrate crystals were also dissolved in acetic acid, although due to bismuth nitrate's low solubility a large quantity of acid was used without achieving total dissolution. The amount of bismuth atoms present exceeded the stoichiometric ratio, by 5%, to titanium atoms to compensate for diffusion of bismuth atoms at high temperature. This was added to the titanium complex in the suba-sealed conical flask, again using a syringe and needle. The suba-seal was then removed and the mixture exposed to air to promote gelling.

While the viscosity of the sol did increase, showing some polymerisation, gelling did not occur. The mixture was dried in an oven, firstly for two hours at 85°C, then for 8 hours at 100°C and finally dried at 300°C for four hours to remove all remaining solvents.

At this point the sample was given the batch code TiP/BiN CH₃COOH to denote its precursors and its method of preparation. The sample was wet milled in a vibromill with a plastic container and agate beads, using methanol as a solvent. This was dried and then passed through a 125µm sieve in order to ensure sufficiently small particle size for good sintering. The sample powder was subjected to thermal analysis, but the results of this were inconclusive.

The powder was pressed into three pellets which were fired for 6 hours at temperatures of 500°C, 600°C and 700°C respectively to obtain information on the optimum firing temperature. These tablets were ground up using a mortar and pestle for examination using the X-ray powder diffractometer, and the results are shown in Chapter 5. The samples were shown to have a low purity of bismuth titanate crystals, so the method was refined.

4.1.2 Second preparation; TiP/BiN HNO₃ (Hydrated)

The second attempt at fabricating a bismuth titanate powder followed the method developed by Sedlar and Sayer more closely [2]. Titanium propoxide was again chelated, however, this time methoxyethanol and acetylacetonone were used in a molar ratio of one part acetylacetonone to four parts methoxyethanol to one part titanium propoxide. Bismuth nitrate crystals were dissolved in nitric acid with four times as much nitric acid as bismuth nitrate crystals by weight. Again the ratio of bismuth atoms to titanium atoms exceeded the stoichiometric ratio, to compensate for the diffusion of bismuth at high temperature. The solutions were mixed and the result was then divided, with one half of the resulting solution having water added to it in the ratio of 10:1 when compared to the original amount of titanium propoxide used, with the other half left unaltered. Both solutions were left uncovered and heated

while stirring was maintained. Though the viscosity of the sols increased, no gel formed. The sample without added water, coded TiP/BiN HNO₃, was dried for 60 hours at 70°C, then 12 hours at 300°C, forming a powder, and vibromilled to reduce particle size and produce a finer powder, to improve the sintering characteristics of the sample. After this it was passed through a 125µm sieve and calcinated at 400°C for 6 hours. The sample with added water, coded TiP/BiN HNO₃ Hydrated, was also dried for 12 hours at 300°C, vibromilled, passed through a 125µm sieve and calcinated at 400°C for 12 hours. The powders were both subjected to thermal characterisation, the results of which provided the firing temperatures of the pellets prepared for examination using the X-ray powder diffractometer. The results of the X-ray characterisation for these were an improvement over those of the first preparation and are presented in Chapter 5.

Due to the hazardous nature of the chemicals involved in this method of preparation, particularly the methoxyethanol and nitric acid, an alternative method using safer chemicals was developed.

4.1.3 Third preparation; TiP/BiN Acac

The final preparation was designed to overcome the drawbacks of the previous method, namely the use of methoxyethanol and nitric acid, both extremely hazardous substances. As with the previous methods, an excess of bismuth was added to compensate for the diffusion of bismuth at high temperature. The titanium propoxide was again chelated with acetic acid, in a molar ratio of 1:4. The bismuth nitrate was dissolved in acetylacetone with a weight ratio of 1:2. The sols were then mixed and the result covered and left to stir. This was then left for 2 weeks to gel, but this did not occur, possibly due to steric hindrance resulting from the comparatively large

size of the bismuth atom or the complexes formed, which reduces the possibility of crosslinking. The sol, which had increased in viscosity without gelling, was dried for 12 hours at 50°C and 6 hours at 100°C. The drying process produced an unexpected result in the expansion of the very viscous sol, shown in figure 1.



Figure 4.1. Result of drying the viscous sol in a standard 115mm diameter dish. As the solvents in the sol evaporated and expanded they were unable to break the surface tension, resulting in an expansion of the sol.

This formation is thought to be the result of bubbles of gas effervescing from the sample, but being unable to break the surface tension of the viscous sol. This material was extremely fragile and collapsed when touched, so the sample was broken down into a powder using a mortar and pestle, before drying for 6 hours at 300°C. The resulting powder was wet milled using a vibromill with agate beads and methanol. The powder was dried before being passed through a 38µm sieve to ensure that the particles would be suitable for screen printing. The powder was then calcinated at 400°C, prompting a colour change from grey to yellow as the impurities

in the sample are burned out. Pellets of the powder were u_{HNO_3} ially pressed at a pressure of 37.69 MPa and then fired at 715°C for between 6 and 24 hours in preparation for thermal and crystallographic characterisation. The results from this sample were very promising, exceeding both the previous preparations, and are presented in Chapter 5.

4.2 Poling

Polarisation, or poling, of the pellets produced is necessary to orient the electric dipoles of the material before it can be used as a piezoelectric and is generally done by applying a high voltage and temperature [4]. The core requirements of heat and high voltage are simple to apply separately, but difficult to apply simultaneously. Two common methods of poling are parallel plate poling and corona discharge poling [5,6]. Apparatus to perform either of these methods was not available so alternative methods were used. Several attempts using different methods were made before the results were successful.

4.2.1 Furnace Poling

The higher the temperature of a ceramic, the lower the voltage required to polarise it. The use of a furnace would allow very high temperatures to be reached, minimising the risk of using high voltage. The initial method used a long probe to hold the sample in the centre of a tube furnace that would both provide heat and act as a Faraday cage. The probe was made of steel and was hollow, allowing wires to be used to apply a voltage to the sample, and a schematic is shown in figure 4.2.

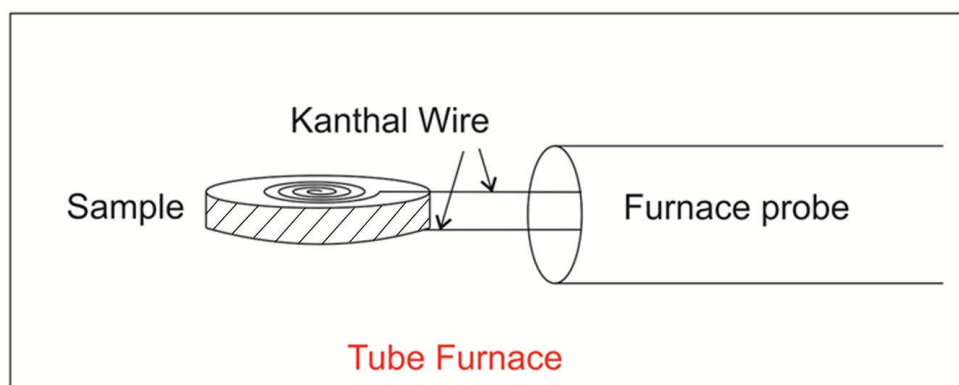


Figure 4.2. Schematic of furnace poling device. The length of the probe and furnace has been omitted, as has the fitting on which the sample and wires rest.

The end of the probe was plugged with a Macor fitting that acted as both a platform for the sample and a fitting for attaching wires to the sample [7]. Two copper wires were threaded through dual-bore alumina tubes down the centre of the probe, to electrically insulate them from each other and from the probe itself. The wires were then threaded through holes in the Macor fitting to bring them in contact with the sample. The wire was clamped to the sample to provide good electrical contacts for the high voltage. Prior to the poling attempts the samples were sputter coated on both sides with a gold-palladium electrode. The initial operational temperature of this method was 700°C, above the Curie temperature of bismuth titanate, with the temperature decreasing while the field was maintained. The plan was that, initially, poling would be attempted with a voltage in the region of 5 kV on samples between one and two millimetres thick, with modifications being made based on the quality of the poling.

In the initial poling experiments the straight contact wires were found to damage the electrodes coated on the samples. This was corrected by forming the

ends of the wires into coils to decrease the risk of damage to the sample and to further improve the electrical contact.

During initial poling tests a short circuit developed within the probe, due to a twist in the wires as they entered the Macor plug. This was corrected and stainless steel discs added to the assembly to prevent copper contamination of the sample from the wires and to evenly spread the pressure from the clamp.

Following these modifications the probe was re-inserted into the furnace and again an electrical short developed. The probe was disassembled and reassembled with Kanthal wire [8], as the copper wire had become brittle due to the high operating temperatures of the probe. The alumina tube taking the wires to the Macor plug was fixed in place with alumina cement in order to eliminate any shorts that may have occurred due to the wires twisting and crossing as they entered the plug; however, the probe continued to develop short circuits at high temperature that were absent at ambient temperature. Ionisation of the nitrogen gas in the furnace was identified as a possible cause for this, so the probe was inserted into the oven with no sample. This “dry run” found no short circuit, leading to the conclusion that ionisation of gas was not to blame for the short circuit, and that the sample itself was responsible. The diffusion of gold in the electrodes on the sample was identified as being a possible source of the electrical short. This hypothesis was given further weight by the presence of gold on the Kanthal wires and the stainless steel discs. The discs were removed, the sample replaced and the wires reversed to remove any gold contamination. However, the probe still short circuited at high temperature implying the continued presence of gold. An alternative hypothesis is that the conductivity of the bismuth titanate is too high at the temperatures used for poling to occur [9]. The metal part of the probe was abrasively cleaned using a silica blaster and the clamp

was removed entirely. The wires were stripped out and replaced, with the replacements holding the sample without need of a clamp. This setup was used to attempt poling of a sample but a defect in the power supply caused the attempt to fail. Although the method appeared promising time constraints forced the focus of the project onto a more standard method.

4.2.2 Oil-Bath Poling

An alternative method of polarisation, oil-bath poling [10], was also investigated. Due to the large amount of experimental difficulty encountered in the initial poling method and the good initial progress into oil-bath poling the focus of the poling trials was shifted.

In oil-bath poling the sample is placed in a bath of heated oil, usually some type of silicone oil, and a voltage is applied to it, as shown in figure 4.3.

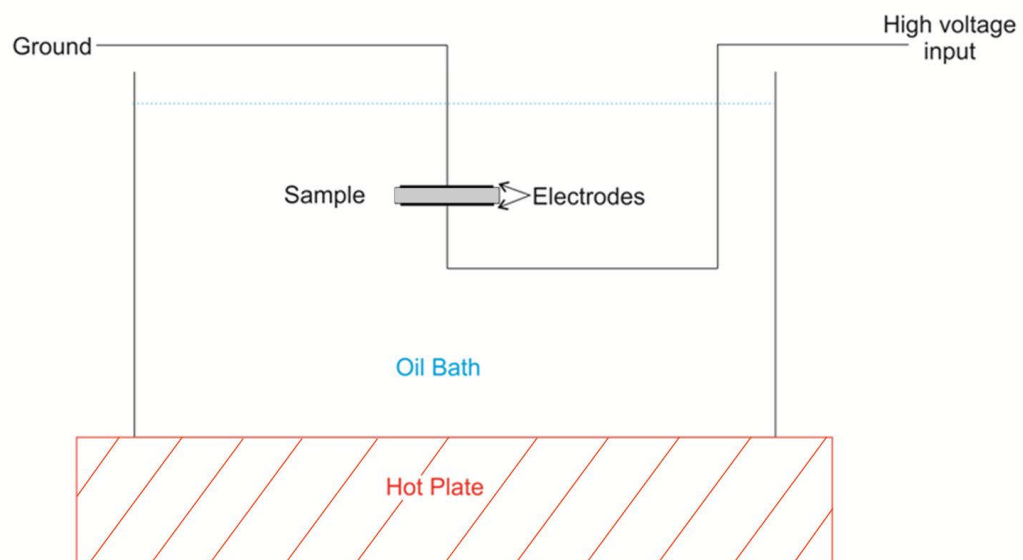


Figure 4.3. Schematic of oil bath poling, with the oil level represented by the dashed blue line. The thermal conduction between the hotplate and the oil bath was quite poor, resulting in sub-optimal poling temperatures.

Transformer oil was identified as a safe and reliable form of silicone oil, with high electrical resistance and thermal stability to approximately 180°C [11]. A high voltage DC power supply was used, capable of generating up to 60kV, although this high a voltage was not used. The heat was supplied by a high temperature hotplate, with temperature limitation due to partial solidification of the oil at temperatures above 180°C and chemical break down at temperatures above 220°C.

As with the previous poling method the samples were sputter coated with gold-palladium electrodes. In addition to this, however, the electrodes were also painted with silver paint in order to attach wires to the sample. Several trials measuring the resistivity of the sample were performed at room temperature using up to 20kV on a 1.76mm thick sample of bismuth titanate. These resulted in the partial destruction of a test sample where arcs formed at the edge of the sample and removed pieces from the edge. As a result the damaged areas of the sample were removed and the electrodes removed from near the edge of the sample. This allowed several successful room temperature characterisations, and finally a polarisation attempt was made. This attempt proved successful, despite lower than optimum poling temperatures. The thermal contact between the hotplate and the Pyrex glass was very poor, so while the hotplate temperatures reached over 300°C the temperature of the oil did not exceed 125°C. The voltage used in the successful poling attempt was 15kV, resulting in a field across the sample of 85kVcm⁻¹. The success of the attempt is discussed in section 6.2.2.

4.3 Fabrication and Characterisation of Thick Films

In addition to the work on fabricating bismuth titanate tablets for use as piezoelectric transducers, growth of thick film transducers for permanent installation was also investigated. The thick films were created by mixing the unfired bismuth titanate powder with a binder and diluant [12] and then applying them to a substrate using a screen printer. The binder is a polymer which binds the powder together and the dilutant is used to regulate the viscosity of the ink, giving a pseudoplastic paste. The screen printing itself uses pressure to force the ink through a very fine mesh onto the substrate [13]. The size of the mesh is dictated by the maximum size of the particles in the powder. In this case a pre-existing mesh required the filtering of the powder to a maximum particle size of 38 μ m.

The thick films were screen printed onto a stainless steel substrate, dried at 150°C to remove the binder and dilutant, and fired in a belt furnace instead of a conventional furnace [13], due to their much lower comparative mass. A six zone furnace was used with temperatures as shown in the table 3 in order to reduce the time spent waiting for a conventional furnace to reach the selected temperature.

Zone 1	Zone 2	Zone 3	Zone 4	Zone 5	Zone 6
300°C	480°C	730°C	730°C	730°C	220°C

Table 3. The temperatures used in the belt furnace, with the sample spending the same amount of time in each zone.

The belt speed was set to 100mm per minute, resulting in a total firing time of approximately 40 minutes. The temperatures in zones three to five were set higher than required as the heat from these zones tends to bleed into the cooler surrounding

zones, reducing their temperature. Measurements of these films are presented in Chapter 5.

References

1. "Piezoelectric thick bismuth titanate/lead zirconate titanate composite film transducers for smart NDE of metals" Kobayashi, M., Jen, G., *Smart Materials & Structures* **13**, Issue 4, 2004, Pages 951-956
2. "Structural and electric properties of ferroelectric bismuth titanate thin films prepared by sol gel method" Sedlar, M., Sayer. M., *Ceramics International* **22**, 1996 Pages 241-247
3. Anton Paar High-Temperature Oven-Chamber: HTK 1200N Specification, Accessed 12/04/2011, http://www.anton-paar.com/High-Temperature-Oven-Chamber-HTK-1200N/X-ray-Structure-Analysis-XRD/60_UK_en?product_id=278#Specifications
4. "Ferroelectric, dielectric and piezoelectric properties of ferroelectric thin films and ceramics" Damjanovic, D., *Reports on Progress in Physics* **61**, 1998, Pages 1267–1324
5. "Piezoelectric thick film ultrasonic transducers fabricated by a sol-gel spray technique." Kobayashi M., Olding T.R., Sayer M. and Jen C. K., *Ultrasonics* **39**, Issue 10, 2002, Pages 675-680
6. "Influence of different poling methods on the second-order nonlinearity in fused silica glasses." Xu, Z., Liu, L., Hou, Z., Yang, P., Liu, X., Xu, L., Wang, W., Affatigato M. and Feller S. *Optics Communications* **174**, Issues 5-6, 2000, Pages 475-479

7. Macor Machinable Ceramics Specifications, Manufacturers Website, Accessed 12/04/2011, <http://www.precision-ceramics.co.uk/macor.htm>
8. Kanthal Furnace Wire Specifications, Manufactures Website, Accessed 12/04/2011, <http://www.kanthal.com/products/materials-in-wire-and-strip-form/wire/resistance-heating-wire-and-resistance-wire/>
9. “Estimation of ionic and hole conductivity in bismuth titanate polycrystals at high temperatures” Takahashi, M., Noguchi, Y., Miyayama, M., Solid State Ionics **172** Issues 1-4, 2004, Pages 325-329
10. “The study of poling behaviour and modelling of cement-based piezoelectric ceramic composites” Dong, B., Xing, F., Zongjin Li, Z., Materials Science and Engineering: A **456**, Issues 1-2, 2007, Pages 317-322
11. Xiameter PMX-561 Transformer Liquid Specifications, Manufacturers Website, Accessed 12/04/2011, <https://www.xiameter.com/en/Products/Pages/ProductDetail.aspx?pid=01496204&R=X222EN&C=US>
12. Supplied by Gwent Electronic Materials, Accessed 12/042011, <http://www.gwent.org/Gem/index.html>
13. “Screenability and Rheology” Miller, L.F., Solid-State Technology **17**, 1974, Pages 54-60
13. Metritherm Nitrogen Belt Furnace, Manufactured by Metritherm Furnace Systems

5. Characterisation of Bismuth Titanate Samples Produced Using Sol Gel Techniques

This chapter presents some of the results of the research; those focused on characterisation of the materials produced. This includes the results from the methods outlined in chapter 3; the results of thermal characterisation, the results of x-ray characterisation and the results of examining the thick films using a microscope.

5.1 Thermal Characterisation

The thermal characterisation used for these materials consists of two distinct methods; differential scanning calorimetry and thermogravimetric analysis. These analyse the heat capacity and the weight of the sample as temperature varies and are described in section 3.1. All of the samples examined in this section have been calcinated at 400°C. These measurements were done using small amounts of powder, in the region of 0.03g. Before being placed in a platinum-rhodium crucible this powder was tested to 900°C on a scrap piece of platinum-rhodium to ensure that the platinum was not damaged by the sample. The sample to be characterised was then heated to 900°C at a rate of 10°C per minute and cooled back to room temperature at the same rate. The powder used for this characterisation was not recoverable.

5.1.1 Thermogravimetric analysis

Figure 5.1 shows the weight loss for the sample coded TiP/BiN HNO₃, described in section 4.1.2.

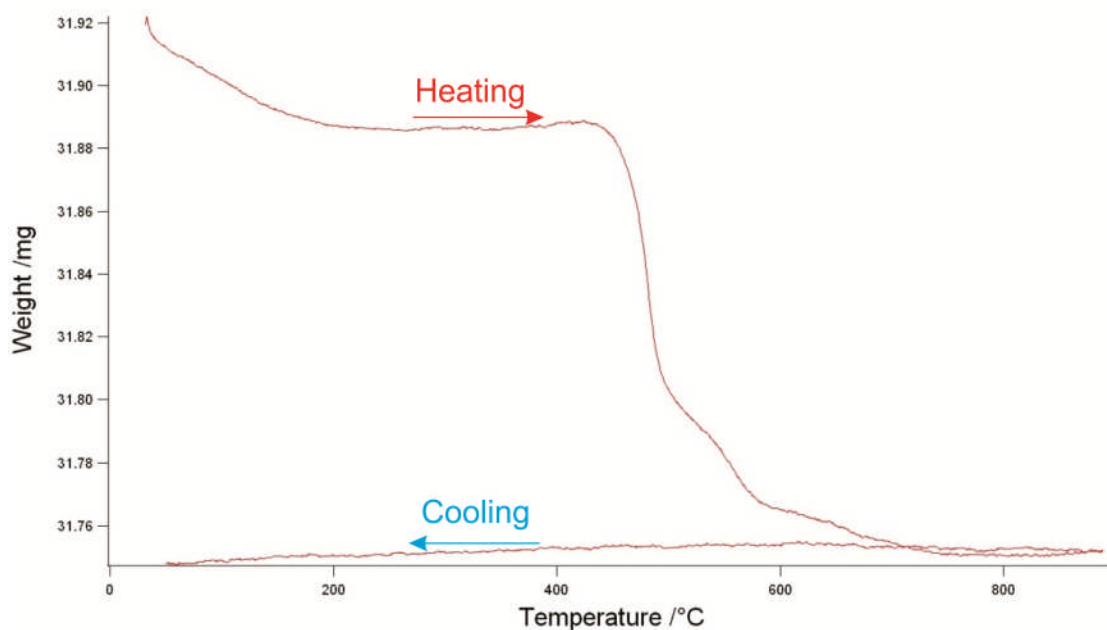


Figure 5.1 Weight loss against temperature for the TiP/BiN HNO₃ sample, showing a gradual initial weight loss up to 450°C followed by a sharp weight loss.

This graph shows a gradual weight loss on heating until the sample reaches 450°C, above which a rapid weight loss occurs. This weight loss stabilises again when the sample reaches approximately 700°C and remains stable for the remainder of the heating data, and through all of the cooling data. The initial weight loss below 200°C indicates loss due to solvents, such as alcohol and water, evaporating from the sample. The subsequent weight loss from 450°C implies that a chemically bound heavier organic has been burned out of the sample. The relatively stable weight of the sample at temperatures above 700° and during the cooling phase of the data acquisition indicates that whatever process caused the weight loss in the sample starting at 450°C had finished, with the slight variation in weight being due to experimental error in the measurement. The total weight loss in the sample was 0.172mg, or 0.5% of its initial weight.

The weight loss graph for the sample coded TiP/BiN HNO₃ Hydrated is similar in shape to the graph shown in figure 5.1 and is shown in figure 5.2.

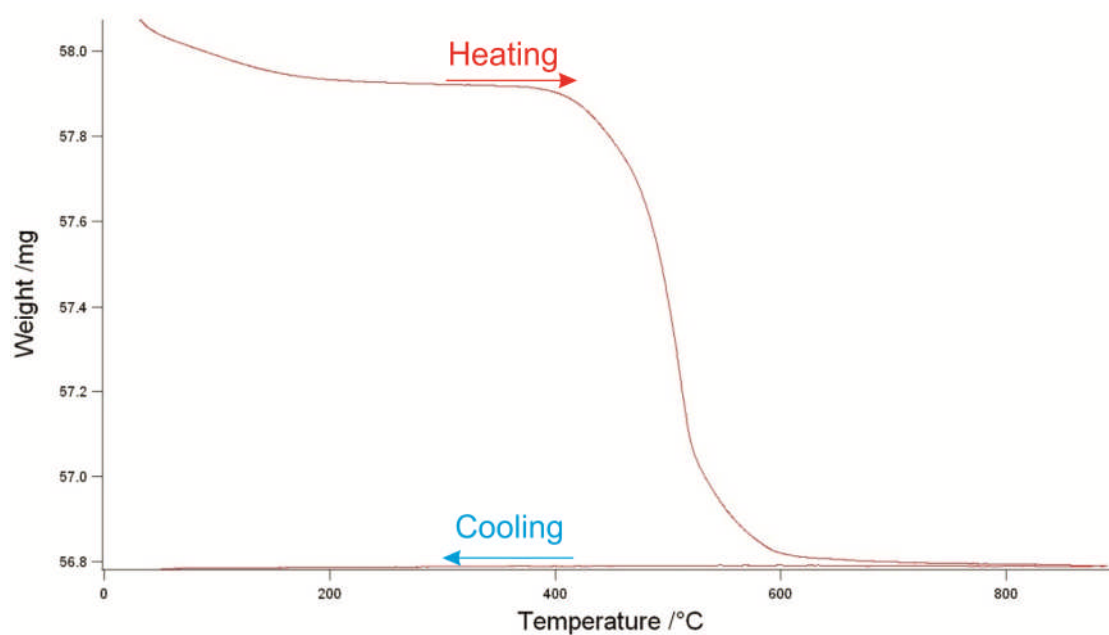


Figure 5.2 Weight loss against temperature for the TiP/BiN HNO₃ Hydrated sample, showing a similar, gradual weight loss followed by a rapid weight loss from roughly 400°C.

As with the previous graph there is gradual weight loss before 200°C, indicating evaporation of water and other organic solvents from the sample. Further, the more rapid weight loss from 400°C again indicates that chemically bound heavier organics are burned out in the later stage, although in this sample it occurs at a slightly lower temperature. This change is most likely due to the changes in sample composition due to the addition of water when it was prepared. As in the previous figure the stability past this point indicates that the removal of organic compounds is complete.

The total weight loss of the sample is 1.288mg, or 2.2% of the original weight of the sample. This indicates that the unfired powder of the first sample contained fewer heavy organics than the second prior to the heating and cooling cycle.

5.1.2 Differential Scanning Calorimetry

The other source of thermal data on the samples is the differential scanning calorimetry (DSC) carried out simultaneously with the thermogravimetric analysis detailed in section 5.1.1, and this technique was described in section 3.1. Figure 5.3 shows the results from the TiP/BiN HNO₃ sample.

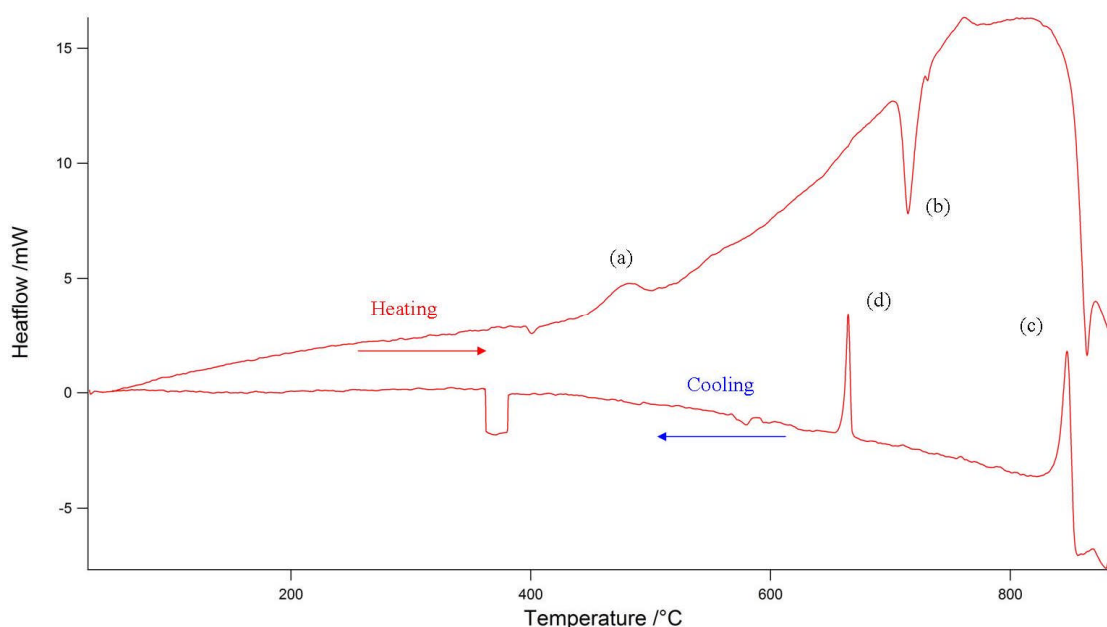


Figure 5.3 DSC data from the TiP/BiN HNO₃ sample, showing heatflow against temperature.

This data shows several interesting characteristics, which are labelled (a)-(d). The discontinuous feature at 380°C on the cooling data is caused by an error in the measurement. Figure 5.4 shows enlargements of the plot in the vicinity of these features.

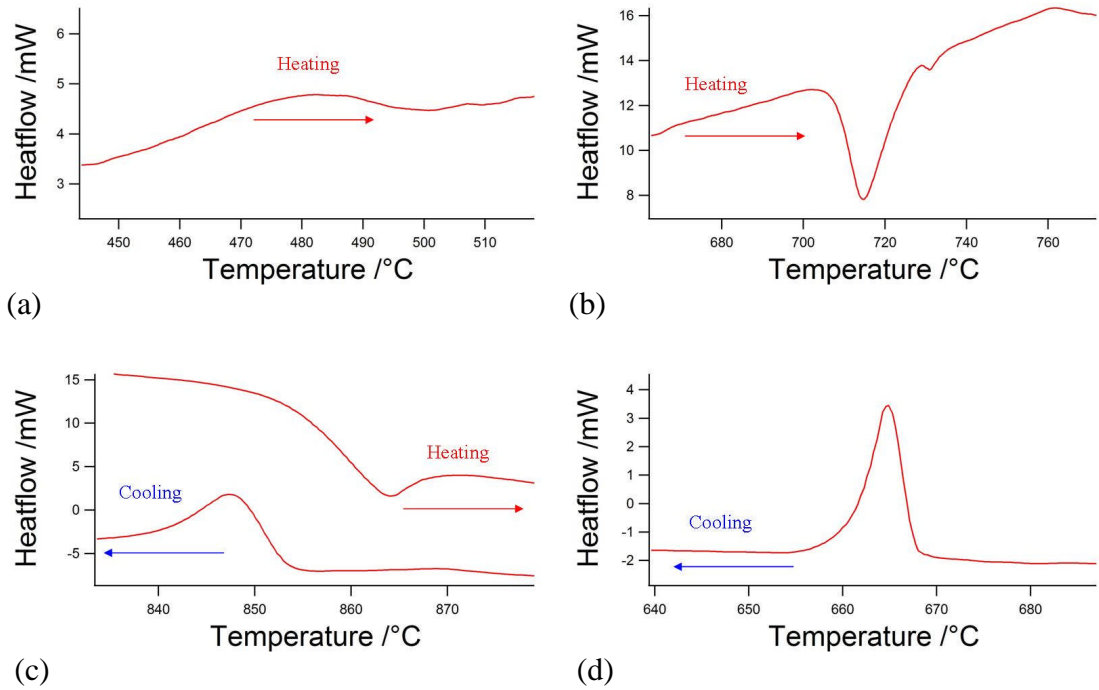


Figure 5.4(a) Enlargement of a broad peak at approximately 480°C (b) Enlargement of crystallisation peak at 715°C (c) Enlargement of the crystal transition at 664°C (d) Enlargement phase change between 840°C and 870°C.

The feature shown in figure 5.4(a) is a peak indicating the formation of bismuth titanate ($\text{Bi}_4\text{Ti}_3\text{O}_{12}$). The broadness of the peak indicates that this process is gradual, occurring over a range of temperatures [1].

Figure 5.4(b) shows an exothermic peak that indicates the transition of the bismuth titanate crystal to a different phase and corresponds to the Curie transition, occurring at 715°C. The features shown in figure 5.4(c) are higher order phase transitions occurring in both the heating and cooling data which were not investigated in this work. The feature in figure 5.4(d) is a phase transition on the cooling data. It corresponds to the transition from a tetragonal structure at high temperature to an orthorhombic structure at lower temperatures. This is the Curie transition of the bismuth titanate crystal and occurs at 664°C [1]. The difference

between the Curie temperatures during heating and cooling is due to the lack of sintering in the unfired sample.

The second set of DSC data was obtained for the sample coded TiP/BiN HNO₃ Hydrated and is shown in figure 5.5. There are several notable features on this graph, and these are shown enlarged in figure 5.6.

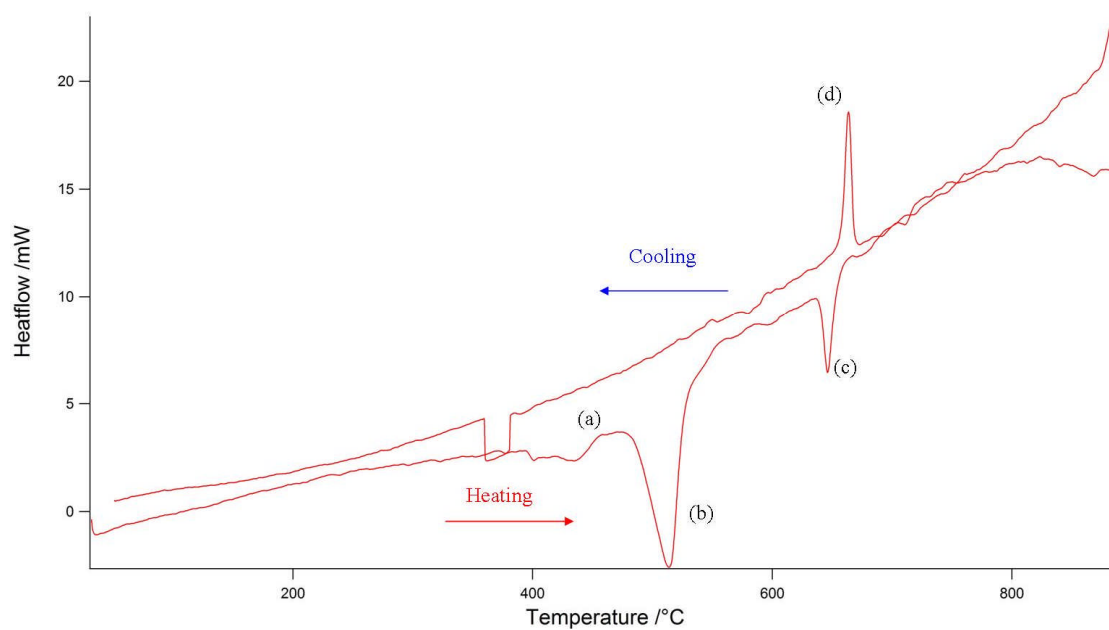


Figure 5.5 DSC data for the sample coded TiP/BiN HNO₃ Hydrated

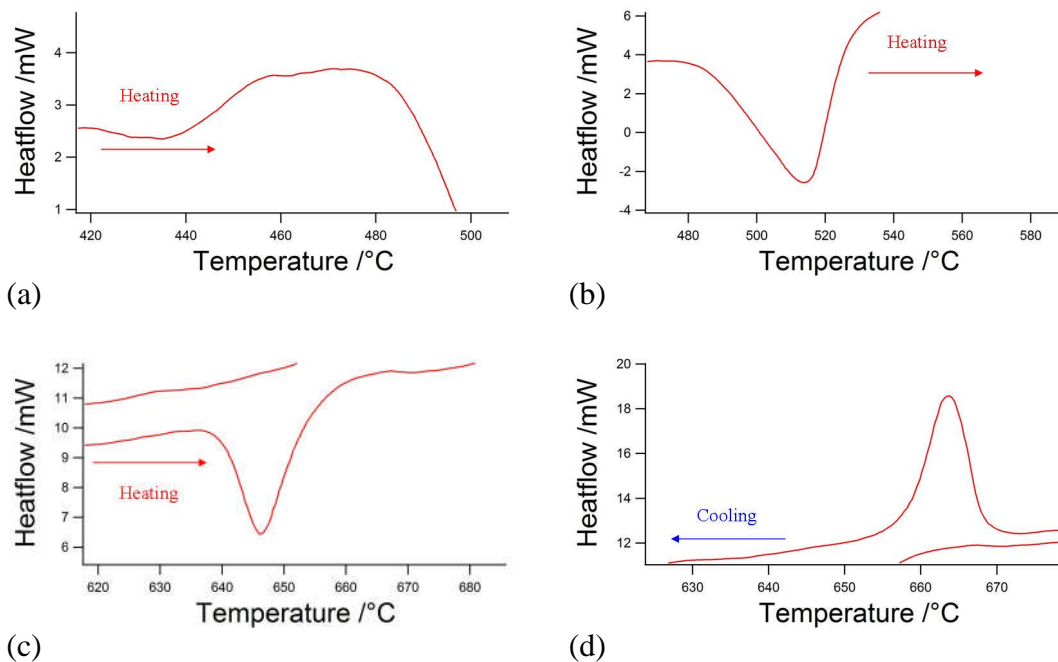


Figure 5.6(a) Enlargement of the formation of bismuth titanate (b) Enlargement of the change in crystal structure of the bismuth titanate (c) Enlargement of crystal transition at 646°C (d) Enlargement of the crystal transition peak at 664°C

Figure 5.6(a) shows an enlargement of a peak which appears to be consistent with the feature shown in figure 5.4(a). As with the TiP/BiN HNO₃ sample, the feature is due to the formation of bismuth titanate [2]. The feature shown in figure 5.6(b) is an endothermic peak which occurs at 516°C, and is likely due to the change of bismuth titanate of one crystal structure to another, that of Bi₂Ti₂O₇ to Bi₄Ti₃O₁₂. This is likely due to the addition of water to the sample during preparation. The feature shown in figure 5.6(c) corresponds to the Curie transition of the material which occurs at 646°C. Figure 5.6(d) shows the crystal transition on the cooling data relating to the Curie temperature of the sample at 664°C. The temperature identified for this peak is within 1°C of the data from the previous sample.

The results shown in figures 5.3 and 5.5 have many similarities; the formation of bismuth titanate occurs at similar temperatures in both and the peak indicating the

Curie transition at 664°C on the cooling data is present in both. The reason for the difference in temperatures of the Curie transitions on the heating data on both samples is not known. The agreement between the cooling data of both samples implies that the most accurate measurement of the Curie temperature from this data is from the cooling data. This measurement is 664°C, which is slightly lower than the accepted value of 675°C [1], although the reason for this is not known.

5.2 Crystal Characterisation using X-ray Diffraction (XRD)

The quality of the samples produced during this experiment was assessed using XRD measurements after the samples had been fired. These measurements were compared to a reference pattern for bismuth titanate, and this is shown in figure 5.7, obtained by simulating the pattern using the lattice parameters in reference [3].

The peaks shown in figure 5.7 provide a reference pattern against which the experimental data can be compared. The reference pattern was obtained at room temperature, as was all of the data presented in section 5.2.1. As with all XRD data the angle on the bottom axis corresponds to the value of 2θ as explained in section 3.2.

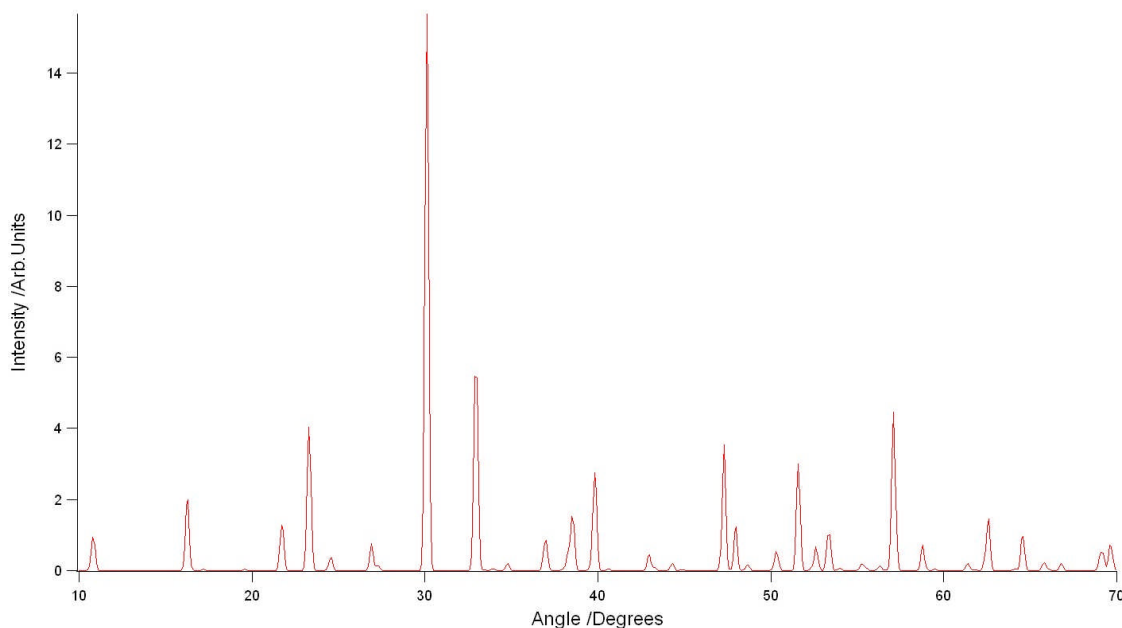


Figure 5.7 Reference XRD pattern for bismuth titanate, $Bi_4Ti_3O_{12}$ [3].

The samples were fired at a temperature identified by the results of DSC/TGA measurements, 715°C (section 5.1.2), for a variety of times, ranging from 6 to 24 hours, to compare the effect firing times had on the purity of the tablet. Once fired the tablets were ground into a powder using a mortar and pestle. The samples were then packed into an aluminium disc, used as a spacer due to the small volume of powder, before being mounted into a larger sample holder and placed in the X-ray diffractometer.

The 2θ parameter was initially varied between 10° and 100°, although this was reduced to 10° to 70° in order to maximise the detail of the scans and reduce the time taken to perform them; none of the data beyond 70° was used and the new range led to the sacrifice of angular range in favour of accuracy and detail. In addition to the standard X-ray diffraction, the high temperature nature of this project required the use of high temperature XRD measurements to examine the behaviour of the sample at and above its intended operating temperatures. In order to facilitate this, a

customised furnace was used inside the diffractometer [4]. The furnace allowed the sample to be heated and to remain at temperature while an x-ray scan was performed. Initially, samples were ramped to target temperatures of up to 700°C at 5°C per minute and allowed to stabilise for 10 minutes before beginning an x-ray scan. Analysis of this data showed that this was insufficient time for the samples to reach thermal equilibrium, so later samples were left one hour before commencing a scan.

5.2.1 Room Temperature X-ray Powder Diffraction

The first sample to be examined using this method was the sample coded TiP/BiN CH₃COOH, with preparation described in section 4.1.1. The x-ray pattern produced is shown in figure 5.8.

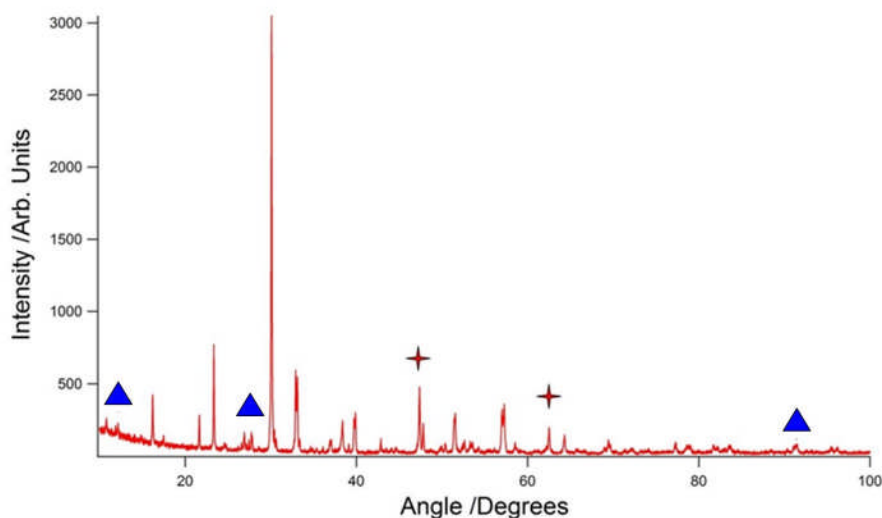


Figure 5.8 The x-ray diffraction pattern measured at room temperature of the TiP/BiN CH₃COOH sample, which had been fired at 700°C for 6 hours. The largest impurity peaks have been indicated, with the blue triangles representing a Bi₂O₃ impurity and the red crosses representing a TiO₂ impurity.

The figure shows sharp, well defined peaks, indicating good crystallisation in the sample. Many of the peaks in the sample correspond to $\text{Bi}_4\text{Ti}_3\text{O}_{12}$ peaks visible in the reference pattern. The low angle background, an artefact of the measurement, can be observed as a gradual slope up to an angle of 20° .

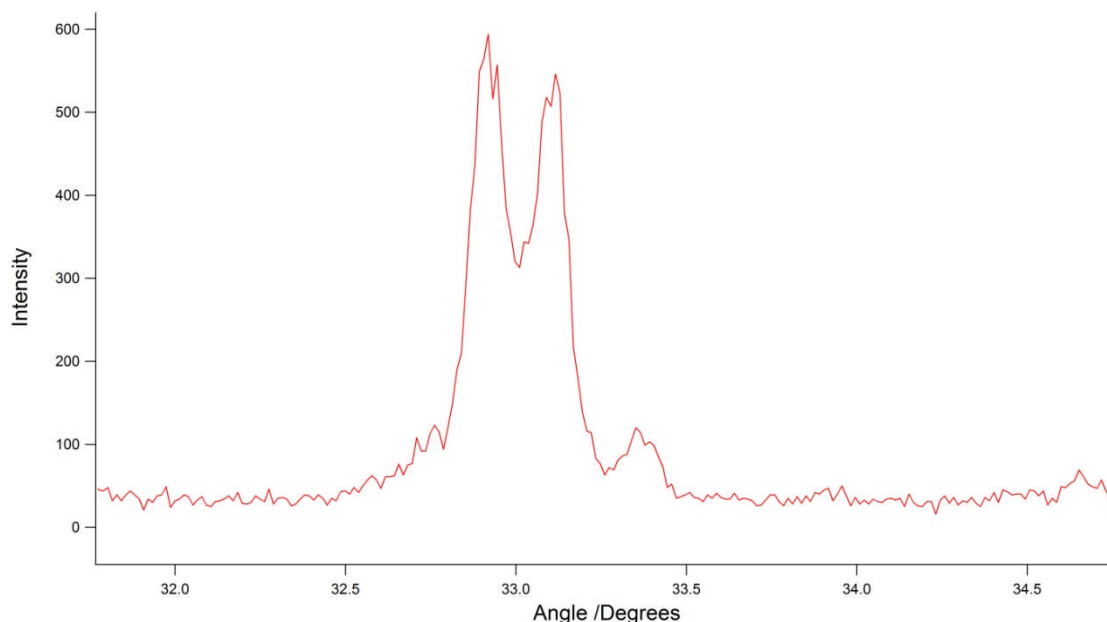


Figure 5.9 Peak splitting due to a shift in the lattice parameters.

Figure 5.9 shows a zoom-in of a section of the data showing three peaks, where only a single peak is visible in the reference pattern. While only a single peak is visible in the reference pattern there are in fact 3 peaks which overlap to produce the single visible peak. That the 3 peaks are distinct in the laboratory produced samples indicates a small change in the lattice parameters of the sample. This could be due to stress distorting the structure or impurities enlarging it.

The second sample to be examined using XRD measurements was the sample coded TiP/BiN HNO_3 , as described in section 5.1.2, with results shown in figure 5.10.

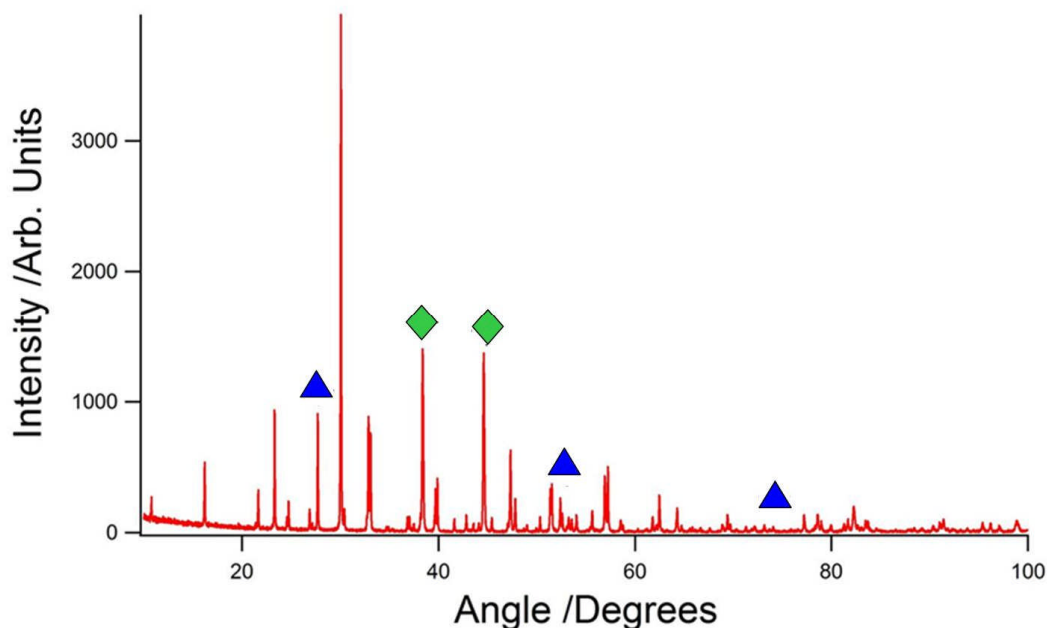


Fig 5.10. X-ray diffraction pattern measured at room temperature of sample coded TiP/BiN HNO₃, which had been fired at 715°C for 24 hours. The impurities have again been indicated, with the green diamond corresponding to the aluminium sample holder and the blue triangle to Bi₂O₃.

The peaks of the pattern are noticeably sharper than those in figure 5.8. This indicates improved crystallinity of Bi₄Ti₃O₁₂ when compared to the TiP/BiN CH₃COOH sample. The positions of the peaks are also closer to those shown in the reference pattern in figure 5.7. The low angle background is still clear in figure 5.10. The aluminium peaks in the data are due to the sample holder and are not relevant to the experimental data.

The third sample characterised was the sample coded TiP/BiN HNO₃ Hydrated, as discussed in section 4.1.2, with results shown in figure 5.11.

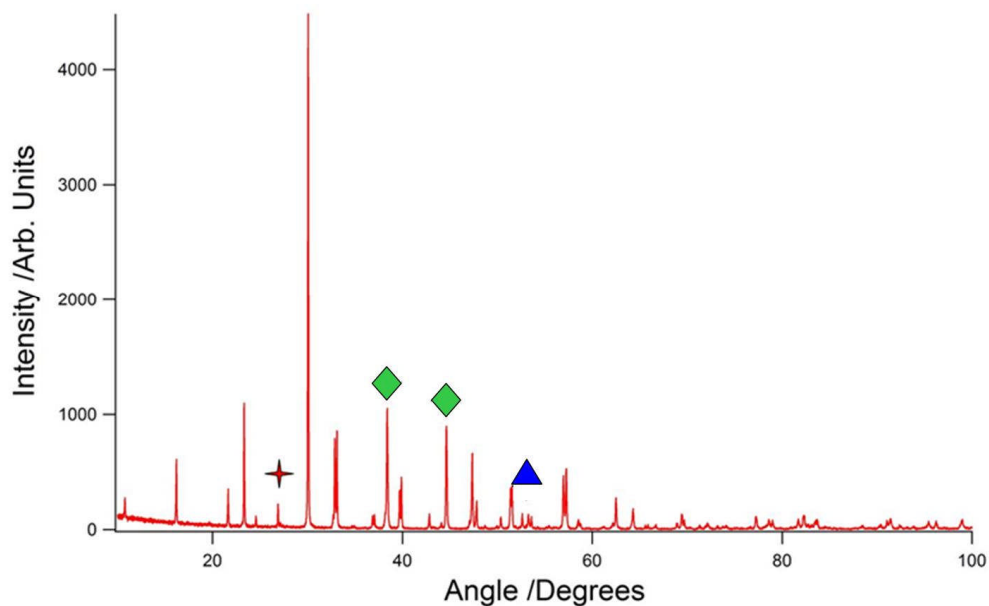


Figure 5.11 X-ray diffraction pattern measured at room temperature of the sample coded TiP/BiN HNO₃ Hydrated, which had been fired at 715°C for 24 hours. The impurities have again been indicated, the red cross corresponding to TiO₂, the green diamond to the aluminium sample holder and the blue triangle to Bi₂O₃.

The diffraction pattern shown in figure 5.11 shows further improvement over the previous two samples, with improved purity shown by the presence of fewer peaks which are not present in the reference pattern. The pattern again shows the distinctive peak splitting observed for the previous two samples, caused by small changes to the lattice parameters of the crystal when compared to the reference sample.

The final laboratory prepared sample to be examined in this way is the sample coded TiP/BiN Acac, as discussed in section 4.1.3, with results shown in figure 5.12.

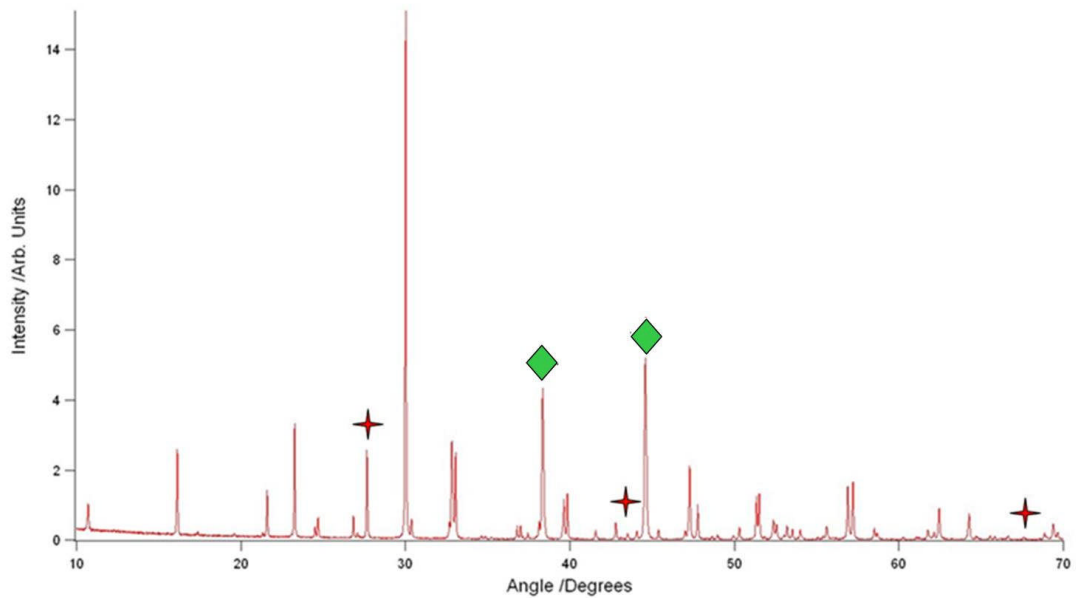


Figure 5.12 X-ray diffraction pattern measured at room temperature of the sample coded TiP/BiN Acac, which had been fired at 715°C for 24 hours. The impurity peaks have been indicated, with the red cross representing a $\text{Bi}_{12}\text{O}_{20}\text{Ti}$ impurity and the green diamonds representing the aluminium sample holder.

As with the previous patterns, figure 5.12 shows strong, well defined crystal peaks, indicating a large proportion of the sample is crystalline bismuth titanate. The evidence of peak splitting also indicates that the dimensions of the crystal are different to those of the reference pattern. The largest other phase in this sample is $\text{Bi}_{12}\text{O}_{20}\text{Ti}$, indicating that the oversaturation of bismuth in the starting precursors, described in section 4.1.3, may have been unwarranted.

In order to make comparisons between the quality of the laboratory prepared powder and bismuth titanate transducers which are available commercially, an x-ray diffraction pattern was taken of a commercial bismuth titanate transducer. This

pattern is shown in figure 5.13, along with the reference pattern and the pattern for sample TiP/BiN Acac.

A very small misalignment of the disc in the centre of the x-ray beam results in a shift along the x-axis of the x-ray diffraction pattern. In figure 5.13 the x-axis offset of the commercial sample has been adjusted to compensate for this and the x-ray patterns have been normalised to the size of the largest peak, present in each sample at 30° . The positive offset along the x-axis of the commercial sample was due to the way the sample was measured, as a solid disc, rather than as a powder. Numerous peaks not visible on the reference pattern are seen in the commercial sample. These correspond to impurities in the commercial sample, such as titanium oxide.

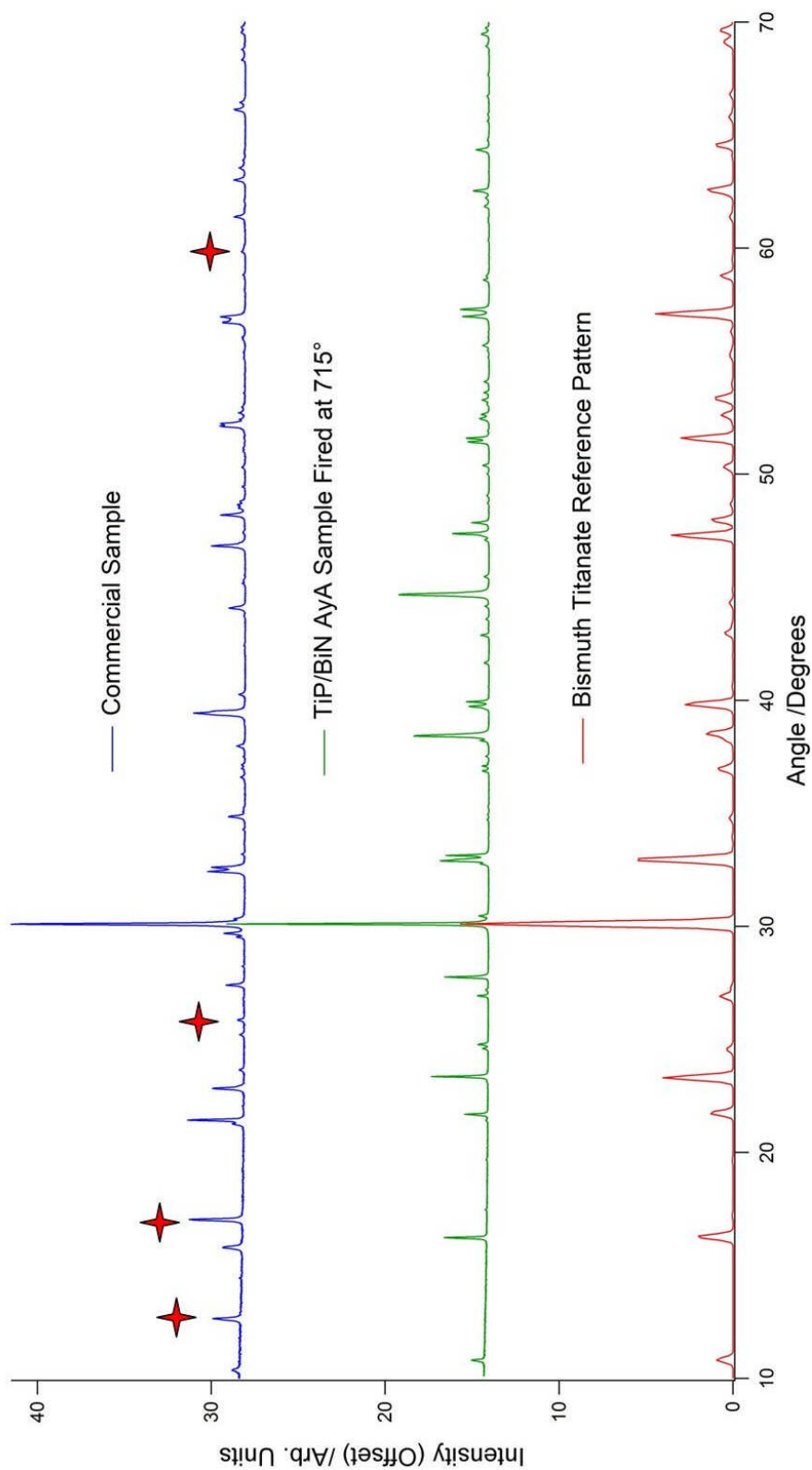


Figure 5.13 Comparison of the reference data, the commercial sample and the sample coded TiP/BiN Acac. The Bi_2O_3 impurity peaks in the commercial sample have been labelled.

The purity of the samples can be estimated by fitting the peaks to existing patterns and comparing their intensities to determine how much of each substance is

present. The accuracy of this measurement is quantified by altering the fits to achieve an extreme value. This is usually done as a preliminary to Rietveld refinement, which is a much more accurate method of identification and uses the diffraction pattern to determine the crystal structure of the sample [4]. This can be used as a highly accurate purity analysis, although the process itself is difficult. Due to the time constraints on the research only a single sample, the sample coded TiP/BiN Acac, was submitted for Rietveld refinement [5]. The purity of the samples is shown in table 4.

Sample	Purity (percentage of $\text{Bi}_4\text{Ti}_3\text{O}_{12}$)
TiP/BiN CH_3COOH	$66 \pm 10\%$
TiP/BiN HNO_3	$79 \pm 10\%$
TiP/BiN HNO_3 Hydrated	$81 \pm 5\%$
TiP/BiN Acac (by simple analysis)	$91 \pm 5\%$
TiP/BiN Acac (by Rietveld refinement)	$87 \pm 1\%$
Commercial Sample	$60 \pm 20\%$

Table 4. Comparison of the purity of the samples examined in this research.

As is evident from the table the crystal purity of the laboratory grown samples is significantly greater than that of the commercial sample. However, due to the offset in the measurements of the commercial sample, its purity could only be obtained to a very poor accuracy. Nevertheless, the samples prepared in this work are of a notably higher purity than the commercially available transducer.

Additionally, the Rietveld refinement of the Acac sample provided lattice parameters for the sample which were different from those obtained from the reference sample, and are detailed in table 5.

Crystal Axis	TiP/BiN Acac Sample	Reference Pattern	Percentage Difference
a	5.41011Å	5.437Å	0.49%
b	5.44840Å	5.426Å	0.41%
c	32.82648Å	32.683Å	0.44%

Table 5. A comparison of the crystal axes for the TiP/BiN Acac sample and those of the reference pattern [3].

Although the difference in the crystal lattice, even as a percentage, is slight, it is of significance. The change in lattice parameters could influence many of the properties of the crystal, from its Curie temperature to its piezoelectric response [6]. However, these crystal lattice parameters are in good agreement with other published values [7].

5.2.2 High Temperature X-ray Powder Diffractometry

In addition to the standard room temperature measurements, several high temperature XRD experiments were conducted. These were conducted on samples which had already been fired, and allowed the crystal structure at high temperature to be examined.

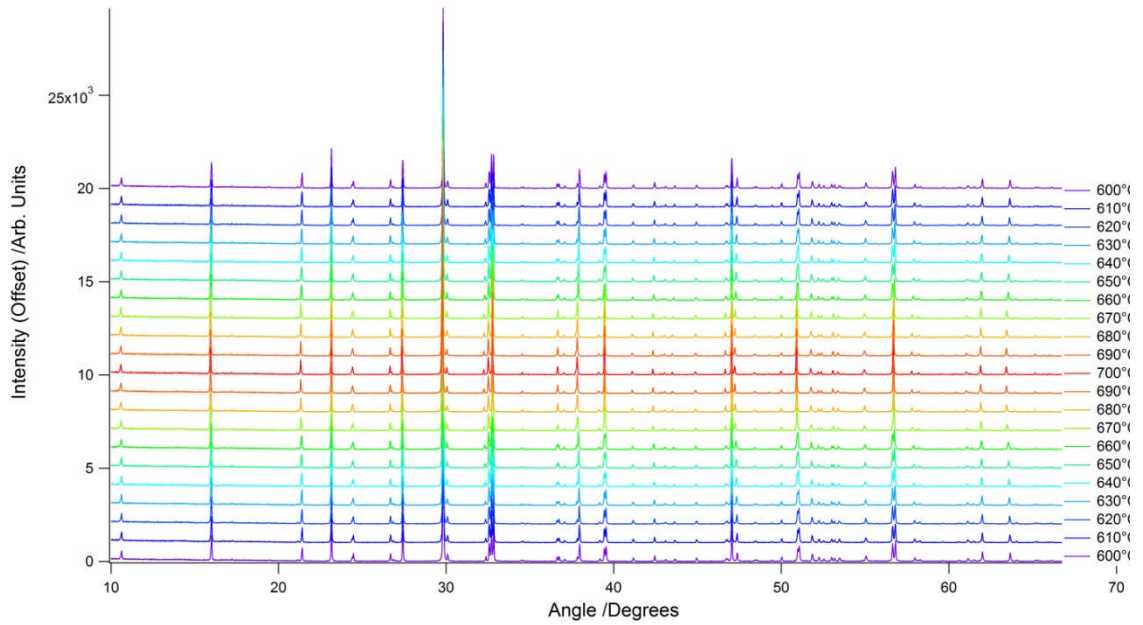


Figure 5.14 High temperature data of TiP/BiN Acac sample, showing the X-ray diffraction patterns of the sample at ten degree Celsius intervals on heating and cooling between 600°C and 700°C.

Figure 5.14 shows the high temperature data for the TiP/BiN Acac sample described in section 4.1.3, which had already been fired at 715°C, between 600°C and 700°C at 10°C steps. This data shows a change in the crystal structure between 660°C and 670°C which is consistent with the Curie transition identified in the DSC measurements presented in section 5.1.2. The data in the region of the Curie transition is shown enlarged in figure 5.15. This is done to highlight the structural difference in the crystal below and above the Curie temperature.

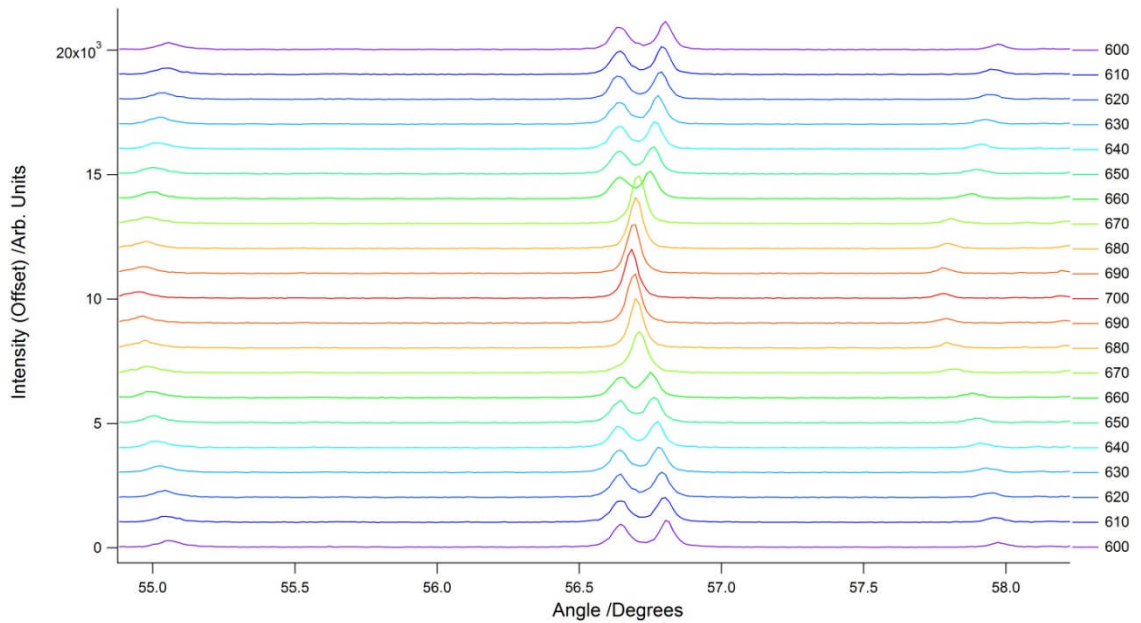


Figure 5.15 Enlargement of the double peaks which form a single peak above the Curie temperature (between 660°C and 670°C). The transition shows the change in the structure of the crystal, from orthorhombic below T_C , to tetragonal above it.

It can be seen in this data that there is a lateral shift in the position of the peaks with temperature. This occurs as the thermal expansion of the sample causes the lattice parameters of the sample to change which results in the lateral shift visible in figure 5.15. It was noted that at the end of some measurements around the Curie transition the sample had a markedly different crystal structure to the start of the scan. This could be due to an insufficient amount of time being left at the end of the heating cycle to allow the temperature of the sample to stabilise, causing the Curie transition to occur during the scan itself. Another possibility is that the higher resolution of the XRD at larger angles allows the peaks to be more clearly resolved. In order to reduce the possibility of temperature shifts during the scan a longer stabilisation time was used for the data shown in figure 5.16, a repeat of the previous

measurement, which also covered a smaller temperature range, from 660°C to 670°C in 1°C steps.

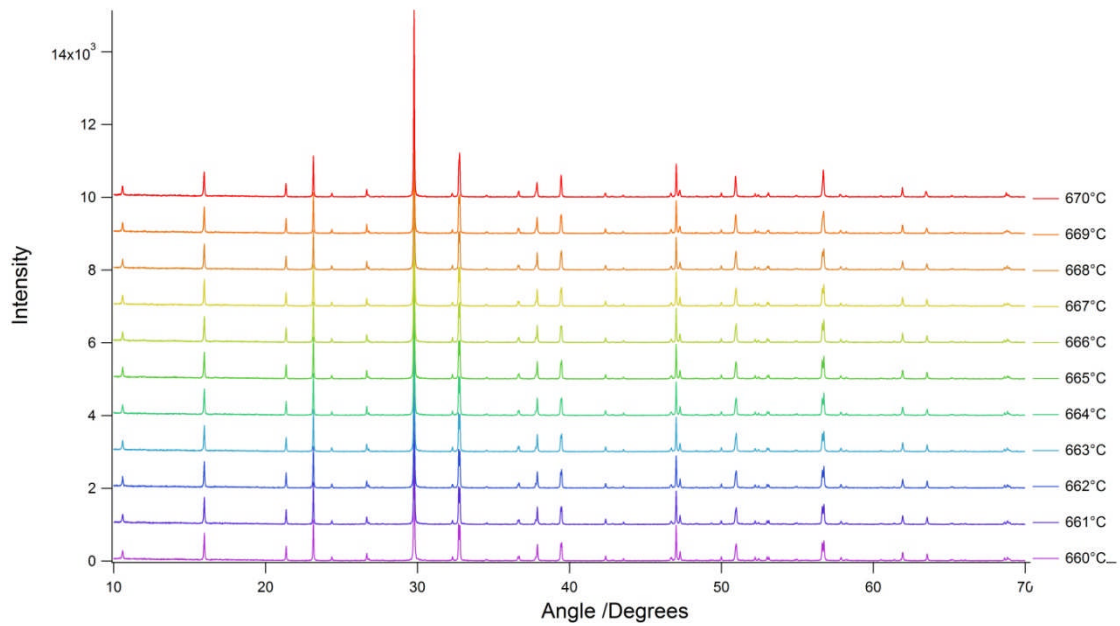


Figure 5.16. X-ray diffraction pattern of the TiP/BiN Acac sample at one degree Celsius intervals.

This data again shows a Curie transition occurring as two peaks between 56° and 57° merge as temperature increases. This region is shown enlarged in figure 5.17. The lateral shift can again be seen in this data, although as the temperature range is smaller, the shift is less noticeable.

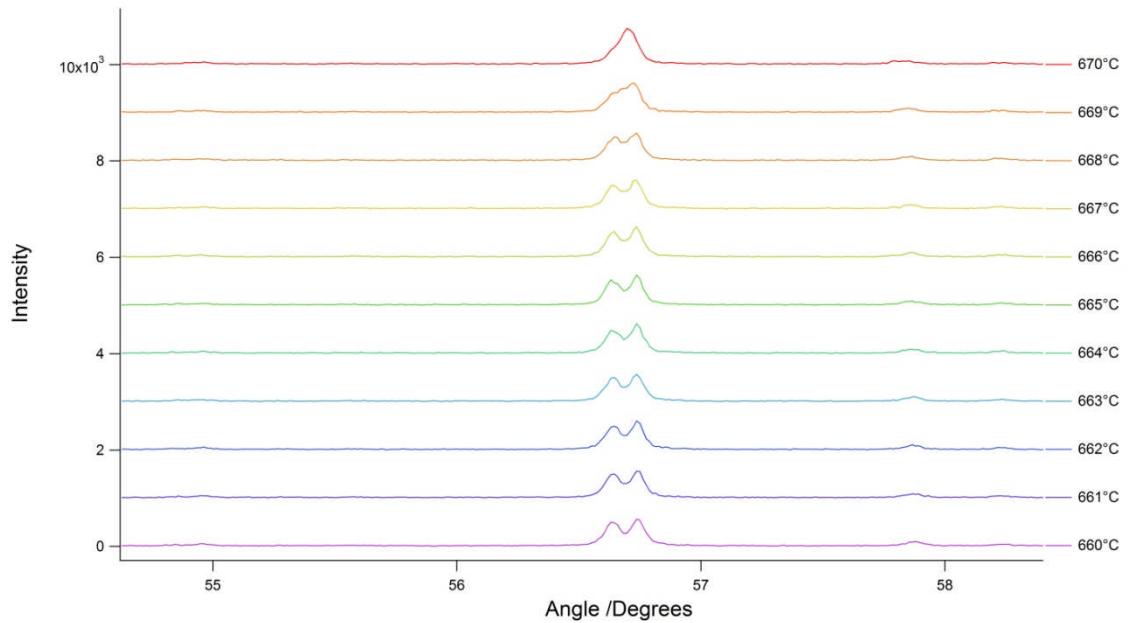


Figure 5.17. Enlargement of the TiP/BiN Acac sample showing the double peaks which merge at the Curie transition to form a single peak. This occurs at some point between 668°C and 670°C

The Curie temperature, $669\pm 1^\circ\text{C}$ found in this method, lies between the previous measurements of 664°C and the reference value of 675°C [1]. This is likely due to the different heating rate used in the X-ray diffractometer when compared to the DSC apparatus. The $\pm 1^\circ\text{C}$ error in the measurement comes from some uncertainty as to where the two peaks converge, limited by the resolution of the detector, which does not take account of the accuracy of the furnace temperature.

5.3 Optical Characterisation Results

The final sample, coded TiP/BiN Acac, was used to fabricate some thick films through screen printing onto a steel substrate. An optical microscope was used to inspect the films and to measure their thickness. The microscope was focused on the substrate and the position of the sample stage set to zero. The stage was adjusted so

that the highest part of the film was in focus and position of the stage was recorded. The sample stage was then moved until the lowest part of the film was in focus and the travel of the stage recorded. The average distance moved by the sample stage between the substrate and the top of the film, and the substrate and the bottom of the film was taken to be the thickness of the film, with the error being the difference between that and the highest value. A diagram of the method is shown in figure 5.18.

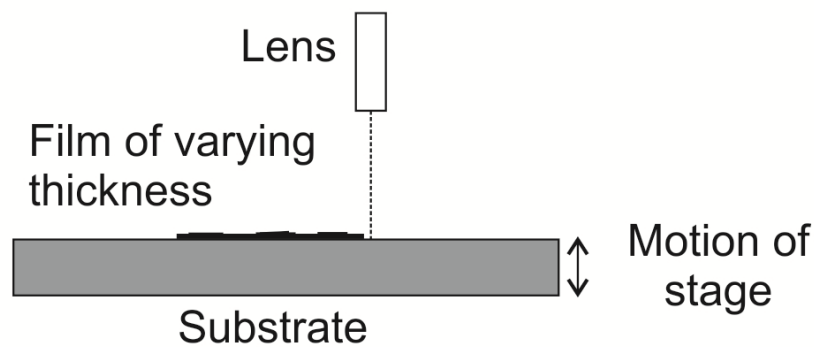


Figure 5.18. How an optical microscope was used to measure film thickness. The position of the sample stage was set to zero when the microscope was focused on the substrate. This allowed the thickness of the film to be measured as the sample stage was moved to focus on the film.

The accuracy of this method will significantly depend on the variation in the thickness of the film. The use of focus to measure the thickness also introduces the possibility of error based on the ability of the operator to focus on the surface of the film.

The images in figure 5.19 show the focus of the microscope on (a) the substrate and on (b) the film.

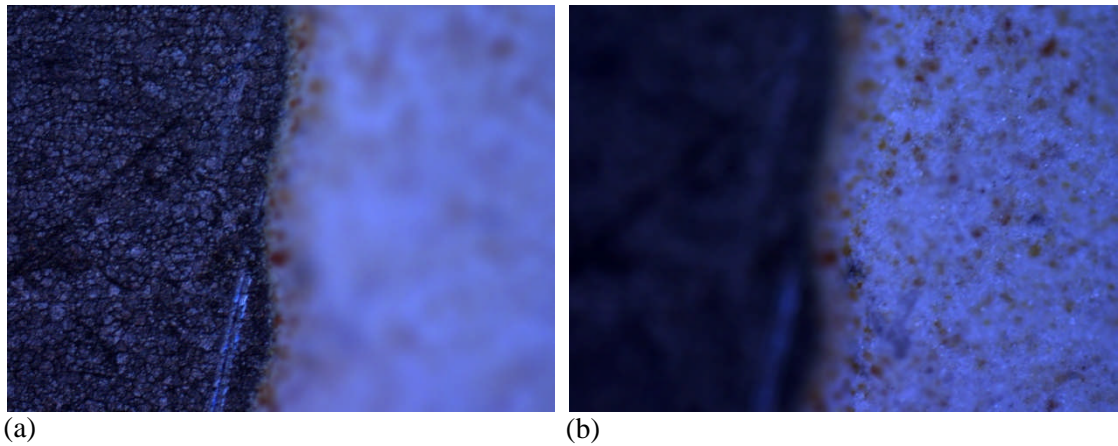


Figure 5.19 (a) Optical microscope image focused on the substrate; (b) Optical microscope image focused on the film. To give a sense of scale, the grain structure of the steel substrate is clearly visible in (a).

These images were used to determine a typical value for the thickness of the sample, which was found to be $21\mu\text{m}$. Using the sample stage height adjuster the microscope the focus was set to the highest and lowest values where the film, which were $25\mu\text{m}$ and $17\mu\text{m}$ respectively. These images are shown in figure 5.20. From these extreme values the thickness of the film can then be stated as $21\pm 4\mu\text{m}$.

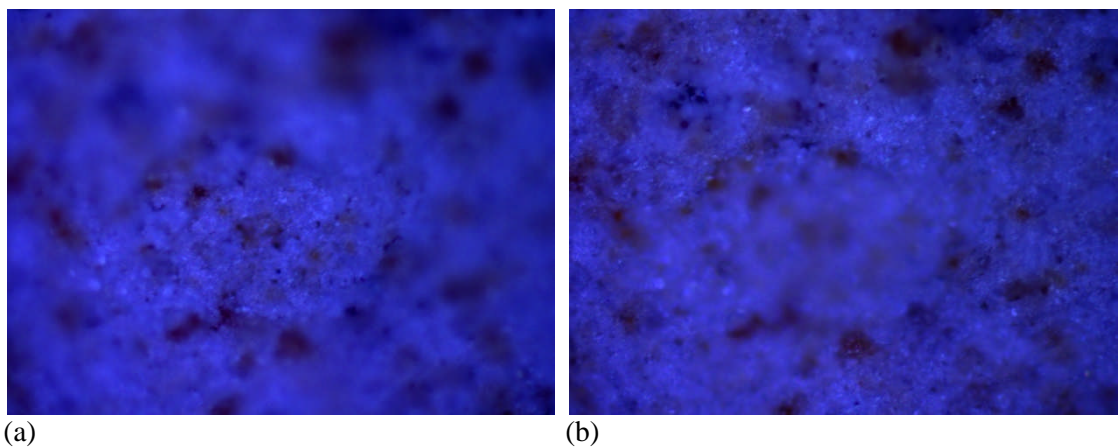


Figure 5.20 (a) Optical microscope image focused on the lowest part of the film; (b) Optical microscope image focused on the highest part of the film.

The optical microscope images also show a reasonably homogenous film free from cracking, although the speckled pattern is unexpected. A possible explanation for the pattern is that the speckles, which appeared yellow under the microscope, represent traces of unreacted bismuth oxide, a yellow chemical.

References

1. "Bismuth titanate from nanocomposite and sol-gel processes" Prasada Rao, A.V., Robina, A.I. and Komarnenia, S., *Materials Letters* **28**, Issues 4-6, 1996, Pages 469-473
2. "Low temperature preparation of ferroelectric bismuth titanate thin films" Xue, K.H., Celinska, J., Paz de Araujo, C.A., *Applied Physics Letter* **95**, Issue 5, 2009, Article Number: 052908
3. "Phase stability in ferroelectric bismuth titanate: a first-principles study" Shrinagar, A., Garg, A., Prasad, R. And Auluck, S., *Acta Crystallographica A* **64**, 2008, Pages 368-375 via Inorganic Crystal Structure Database
4. "A profile refinement method for nuclear and magnetic structures" Rietveld, H. M., *Journal of Applied Crystallography* **2**, 1969, Pages 65–71
5. Reitveld Refinement performed by Iain Dunn, Glass Ceramics group, Department of Physics, University of Warwick
6. "Strong correlation between lattice strains and Curie temperature in $\text{La}_{1-x}(\text{Ca/Sr})_x\text{MnO}_3$ " Tanga, F.L. and Zhang, X., *Computational Materials Science* **40**, Issue 3, 2007, Pages 434-438
7. "Structural basis of ferroelectricity in the bismuth titanate family" Newnham, R.E., Wolfe, R.W. and Dorrian, J.F., *Materials Research Bulletin* **6**, Issue 10, 1971, Pages 1029-1039

6. Characterisation of the Ultrasonic Behaviour of Bismuth Titanate Samples

In addition to the material characterisation results presented in the previous chapter several ultrasonic characterisations were performed. The ultrasonic measurements were performed on the TiP/BiN Acac tablets prepared as described in section 4.1.3, to demonstrate their functionality as transducers.

6.1 Tap Test Measurements

The first test performed on the transducer was a simple tap test, to check the piezoelectric response of the sample at low frequencies. The sample transducer was placed on a metal plate attached to the ground wire of a 10x oscilloscope probe. The main part of the oscilloscope probe was placed on the top of the sample, allowing the oscilloscope to act as a high precision voltmeter across the sample.

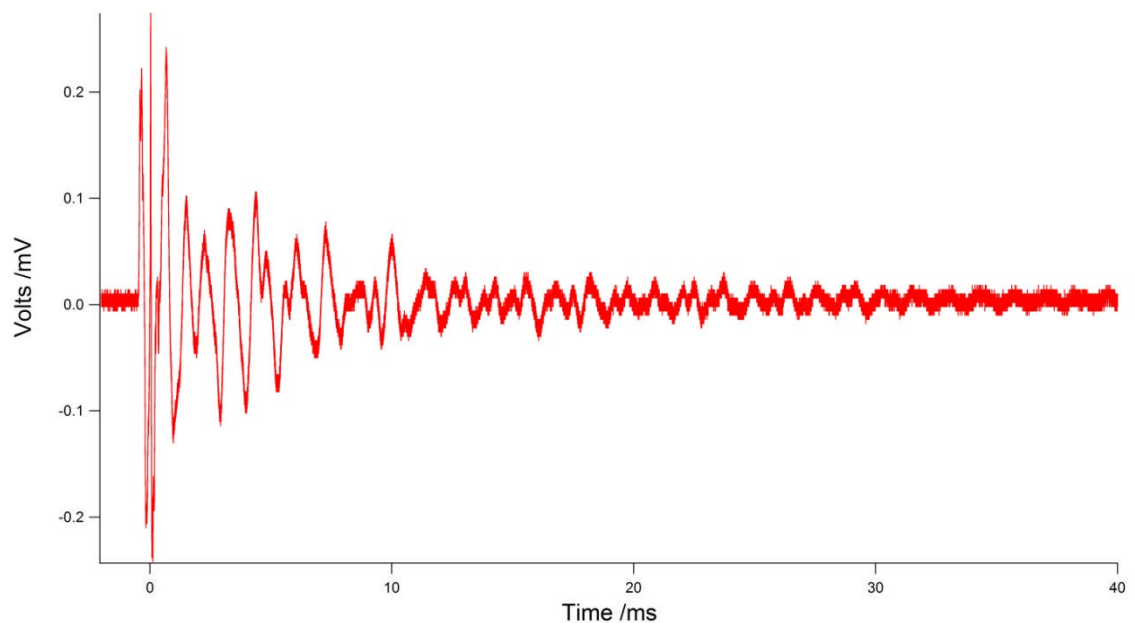


Figure 6.1 The output voltage of a test transducer during a tap-test.

Figure 6.1 shows the signal from the oscilloscope when the sample was struck and clearly shows a piezoelectric response in the sample. The data has a low signal to noise ratio, with a peak of only 13 dB, which could be due to a low piezoelectric response, or, more likely, that the sample is not sensitive in this frequency region.

It is possible to calculate the resonant frequency of the sample by using a fast Fourier transform (FFT) on the data shown in figure 6.1. The FFT of the data shown in figure 6.1 is shown in figure 6.2.

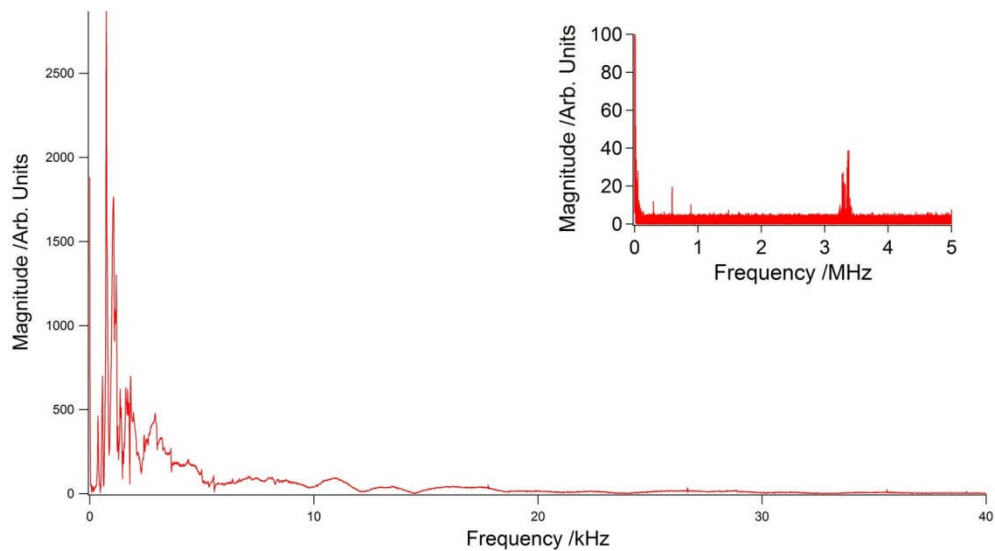


Figure 6.2 Fast Fourier transform or FFT of the data shown in figure 1. This shows a low frequency signal consistent with a percussion of the transducer. The inset shows a wider frequency range for the FFT.

As can be expected there is a large pulse at low frequency due to the percussion. The inset also shows a peak at higher frequencies indicating that the transducer has an increased sensitivity to noise at that frequency. This increase in sensitivity corresponds to the resonant frequency (see section 6.2) and is at $3.35 \pm 0.10\text{MHz}$, as this will be the frequency at which, due to its geometry, the transducer is most sensitive.

6.2 Use of the Sample Transducer for the Generation and Detection of Ultrasound

The next set of measurements that were performed on the tablet transducers were to investigate their functionality as working transducers. The transducers were placed onto a test block of aluminium. Although the transducers were used without the casing or wear plate described in section 1.2.3.3 a standard gel couplant was used between the transducers and the sample. The sample transducer tested had electrodes applied on both sides using silver paint. The measurements performed were thickness tests of the aluminium test block 12.77 mm thick.

Initially these tests were performed using a single ultrasound transducer in pulse-echo mode. However, the transducer failed to produce a reliable ultrasound signal in this setup, likely due to both the lack of damping and the lack of a matching layer into the sample. Subsequently two transducers, one test transducer and one commercially available quartz transducer, of resonant frequency 5 MHz and diameter 12 mm, were used in through transmission mode to allow the sample transducer to act as either generator or receiver independently. The laboratory arrangement for this is shown in figure 6.3.

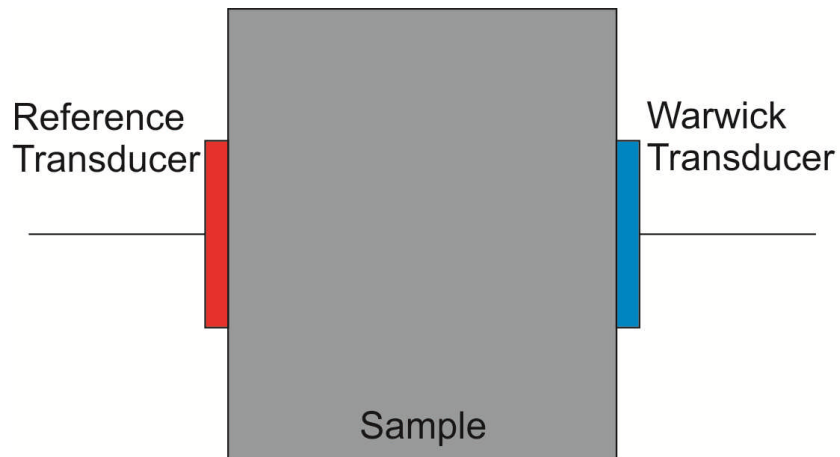


Figure 6.3 Schematic showing the arrangement of transducers in a through transmission measurement. The transducers were grounded to the sample using the electrodes present, with the electrical connection to the signal generator being made by a BNC cable. Note that the reference transducer here is not the commercial transducer used in comparison measurements.

The transducers were arranged as shown in figure 6.3 to allow both transducers to detect the ultrasound signal generated by one of them.

Figure 6.4 shows the response of both transducers as detectors when the commercially available quartz transducer is used as a generation transducer and driven with a Matec 6600 signal generator.

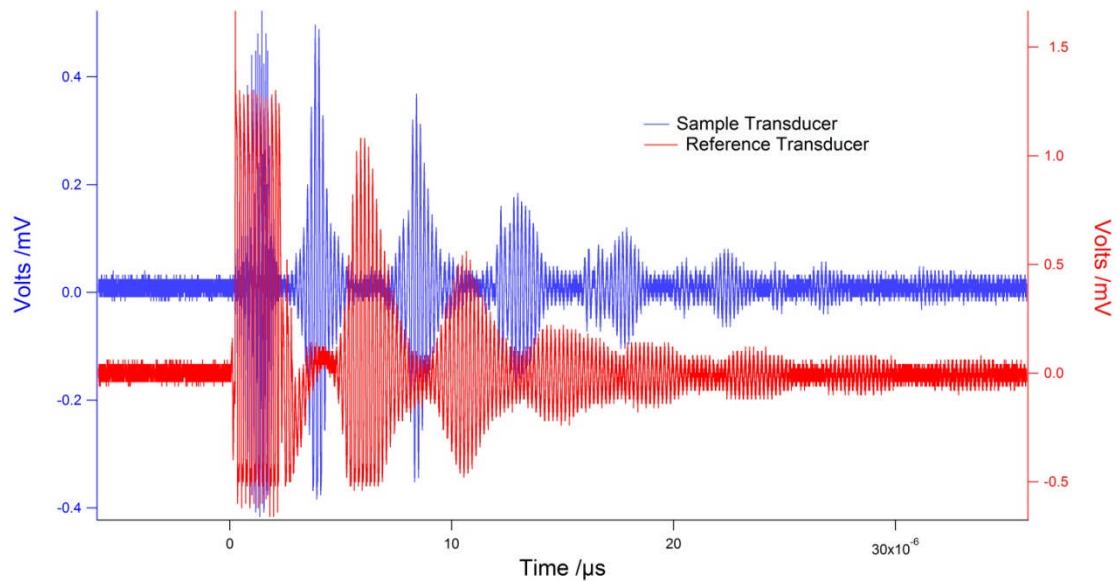


Figure 6.4 The ultrasound data from an oscilloscope obtained from the arrangement of transducers shown in figure 6.3. The red trace represents the data detected by the reference transducer and the blue the data from the sample transducer.

The sample transducer response is shown by the blue line and that of the quartz transducer is shown by the red line. The signal from the quartz transducer was amplified using the built-in amplifier in the Matec 6600 signal generator, while the signal from the sample transducer was amplified using a separate amplifier. This, in addition to the much larger size of the signal, accounts for the presence of clipping in only the quartz transducer signal. The initial generation pulse appearing on both transducers is likely due to crosstalk between them. This will arise from electrical crosstalk through the wires leading to the transducers, or electrical crosstalk through the sample itself. The offset of the remaining pulses is due to the position of the transducers on opposite sides of the sample as shown in figure 6.3. The spread of the signal over time is due to the misalignment of the transducers, one was slightly higher on the sample than the other. This will result in the transducer detecting the echoes from the edges of the test sample caused by the spread of the ultrasound

beam. The decreasing envelope of the signals shows the attenuation of sound in the medium and the distance between the reflections can be used to calculate the thickness of the material.

6.2.1 Aluminium Test Block Thickness Measurements

The time elapsed from peak-to-peak between two echoes is $4.47\mu\text{s}$, with a path length equating to twice the thickness of the sample through which the ultrasound is propagating. Using the speed of sound in aluminium, 6374ms^{-1} [1], the thickness of the sample can be calculated to be $14.7 \pm 0.3\text{mm}$. This is in comparison to the measured value of $12.77 \pm 0.01\text{mm}$ using a micrometer screw gauge.

There are several possible explanations for the discrepancy between these two values. The most likely cause is the inaccuracy when measuring the time between peaks as this will be affected by both noise in the data and by any phase changes during reflection. Another contributing factor is the possibility of a difference in the speed of sound of the aluminium sample and the reference value, due to the use of an aluminium alloy with a speed of sound slightly different to that of the reference velocity, although this would be a very minor effect, as in order to obtain the thickness measured the speed of sound in the aluminium would have to be 5537ms^{-1} .

6.2.2 Transducer Measurements

The final measurement on the sample transducer was an evaluation of its quality as a transducer, by way of a d_{33} measurement. This measurement is a measure of the physical response of a transducer to an applied voltage and is explained in section 2.2. The sample transducer was measured in an APC YE2370A d_{33} meter which gave a d_{33} measurement of $(20.5 \pm 0.7) \times 10^{-12}$ C/N. This was compared to a

commercially available bismuth titanate transducer, which had a d_{33} measurement of $(18.5 \pm 0.7) \times 10^{-12}$ C/N. This is a favourable result and indicates the success of this method when compared to the commercial sample. Other work has produced samples with d_{33} measurements of up to 26×10^{-12} C/N, which indicates that with further research the quality of the samples can be increased further [2]. However, exceeding the standard of the commercial sample is an excellent initial result.

References

1. "Tables of Physical & Chemical Constants. 2.4.1 The speed and attenuation of sound." Kaye & Laby Online. Version 1.0 (2005) www.kayelaby.npl.co.uk Accessed 7/3/2011
2. "Grain-oriented fabrication of bismuth titanate ceramics and its electrical-properties" Seth V.K., Schulze W.A., IEEE Transactions on Ultrasonics Ferroelectrics And Frequency Control **36**, Issue 1, 1989, Pages 41-49

7. Conclusions

This final chapter summarises the key results of the research, an evaluation of the methods used and possible avenues of future work.

7.1 Results and Discussion

7.1.1 Material Characterisation

The analysis of the TiP/BiN HNO₃ and TiP/BiN HNO₃ Hydrated samples (section 4.1.2) via differential scanning calorimetry shows a Curie temperature of 664°C, which is slightly lower than other reported Curie temperatures in the literature [1]. The difference between these values is likely due to the variation in the lattice parameters of the sample used, discussed in section (5.2.1). The analysis via high temperature X-ray diffraction of the TiP/BiN Acac (section 5.2.2) sample shows a Curie temperature of 670°C. This value is in good agreement with the commonly accepted value of 675°C [1].

The highest purity sample, the TiP/BiN Acac sample, contains $87 \pm 1\%$ bismuth titanate, in comparison to the commercial sample's value of $60 \pm 20\%$. The higher purity of the sample produced in this work indicates that the sol-gel method has an advantage over the milled oxide method used to produce the commercial sample. The higher purity sample allows for transducers with higher piezoelectric response as more of their volume will be the piezoelectrically active material.

A pellet of the TiP/BiN Acac sample was poled in a field of 85kVcm^{-1} at a temperature of 125°C, resulting in a sample displaying good piezoelectric response. The tablet transducer tested had a resonant frequency in the region of 3MHz. The

piezoelectric response of the transducer was measured using an APC YE2370A d_{33} meter to find its d_{33} value [2]. This was found to be $(20.5 \pm 0.7) \times 10^{-12}$ C/N, compared to a value of $(18.5 \pm 0.7) \times 10^{-12}$ C/N for the commercially available sample. This is a highly promising result as it indicates that the sample prepared in this work is of a quality that is comparable to commercially available transducers.

Additionally, the preliminary work done on the fabrication of thick films appears promising. The films adhered well to the substrate and were of a reasonably consistent thickness.

7.2 Evaluation of Novel Experimental Methods

Several novel methods for preparing the bismuth titanate were developed during the course of this project. Poling techniques, such as furnace poling, were also explored, with some being more successful than others. These methods are summarised in the following sections.

7.2.1 Novel Sol Gel Method

The novel sol-gel method using acetylacetone, described in section 4.1, worked extremely well in providing fine, homogenous powders that can be fired at lower temperatures than comparable milled oxide powders, to produce purer $\text{Bi}_4\text{Ti}_3\text{O}_{12}$ ceramics. The material characterisation results were given in chapter 5. The second most common substance in the samples, by percentage, was $\text{Bi}_{12}\text{O}_{20}\text{Ti}$. This is the result of an oversaturation of bismuth as a starting precursor and could be corrected by lowering the amount of bismuth nitrate used.

7.2.2 Oil-Bath Poling

The method of oil-bath poling explored is widely used in industry as a means of polarising piezoelectric ceramics. The implementation used in this research produces poled samples capable of being used as ultrasound transducers, although there are several improvements that could be made;

The method of attaching the wires to the sample in the oil bath is an area which could be improved, to increase the efficiency of the method. The wires were attached with silver paint, creating a conductive bond between the wires and the sample. This paint takes 24 hours to dry properly and is very delicate when dry, breaking easily. A possible solution to this problem is to use stiff wires to maintain electrical contact to the sample in the oil instead of the silver paint. This is possible as the current flow in the circuit is very low, and the polarisation of the samples is dependant only on the electric field. Even a poor electrical contact with the sample would be sufficient to polarise it.

Another area that can be improved in the method is increasing the temperature the oil bath is capable of achieving. Currently the heat conduction from the hotplate to the oil is poor, and a hotplate temperature of approximately 300°C is required to achieve an oil temperature of 125°C. In order to obtain higher oil temperatures a purpose built oil bath could be used instead of the hotplate and glass dish used here. However, a maximum temperature is still imposed by the oil itself [3], with higher temperature oils required to raise the oil bath above 200°C.

7.3 Future Investigations

In addition to the work completed so far and the avenues of further work already mentioned there are several paths for further research which could be explored in a longer research project.

7.3.1 Alternative Poling Methods

In addition to the methods of poling examined in this project several others exist. The most common is that of corona poling [4,5]. This is performed by passing high voltage into a needle above a grounded sample. The sample is heated before the voltage is applied, as with all poling procedures, and cooled while maintaining voltage. Another common method is that of parallel plate poling [5]. The sample is placed between two parallel plates and heated. A voltage difference is then applied to the plates, creating an electric field between them. This field is maintained as the heat is removed, poling the sample. The limitations of a one year project precluded the development and implementation of these techniques, although they remain excellent candidates for further work.

7.3.2 High Temperature Experiments

The aim of this full research project this work forms part of is to examine the performance of high temperature transducers, specifically bismuth titanate. In addition to the high temperature characterisation already performed, high temperature ultrasound experiments must be undertaken. These include the measurement of the d_{33} constant for the samples over a range of temperatures to evaluate the effect of high temperatures on the performance of the transducer. This involves measuring the force exerted by the sample for a given charge across the

sample. If the machine used previously to measure the d_{33} constant could be adapted to high temperature use it would be ideal for this; however, this may be extremely difficult due to the adaptations that must be made to correct for thermal expansion. The use of a laser interferometer to measure the surface displacement of the sample at high temperatures as a current is passed through it may be more practical, as the non-contact nature of the measurement would allow the effects of thermal expansion to be ignored.

Ultrasonic measurements must also be taken at high temperature to evaluate the signal to noise ratio of the transducer and to establish a useful upper limit for its operation. These could be performed inside a furnace, using either high temperature couplant or with a sample transducer clamped to a metal block. If thick film transducers were used the need for either couplant or clamping would be removed.

Aging tests must also be performed to evaluate the long-term viability of the transducers. These could be performed by measuring the d_{33} value of a sample at given time intervals while the sample is either held at a high temperature, or cycled from low to high temperatures. These tests would require heating the transducer up to its maximum planned operating temperature, 550°C, for possibly weeks at a time.

7.3.3 Thick Film Experiments

The pellet transducers produced so far were the first towards the production of thick film transducers. The poling of the thick films produced so far must be performed, followed by the examination of their ultrasonic characteristics over a range of temperatures to investigate any differences between them and the pellet transducers. This could be performed in a similar manner to the work described in the previous section.

Additionally, methods of attaching the transducers to samples, either by printing them directly onto the samples to be tested, or by bonding substrates with transducers printed on them onto the samples, must be explored. This could be performed by comparing the operation of both options at a range of temperatures. Field tests using both options should also be performed, to add valuable data on the performance of the samples in a real environment and to compare their real world performance.

7.3.4 Doping

Doping is the intentional addition of impurities to a sample. These impurities can alter the material properties of the sample, altering the Curie temperature or the piezoelectric constant. Substituting some of the metal atoms in the $\text{Bi}_4\text{Ti}_3\text{O}_{12}$ structure for other metal atoms like magnesium [6] or tungsten [7] would be a promising area for continued research. Doping the samples would ideally produce transducers with a higher Curie temperature, although this could be at the cost of making the transducers harder to polarise. The doping agents would be added early in the preparation, when the materials are mixed as a sol, requiring additional preparations of the material.

References

1. "Bismuth titanate from nanocomposite and sol-gel processes" Prasada Rao, A.V., Robina, A.I. and Komarnenia, S., Materials Letters **28**, Issues 4-6, 1996, Pages 469-473
2. American Piezo Wide Range d_{33} Meter, accessed 12/04/2011
http://www.americanpiezo.com/products_services/testers.html

3. Xiameter PMX-561 Transformer liquid specifications
4. "Piezoelectric thick film ultrasonic transducers fabricated by a sol-gel spray technique." Kobayashi M., Olding T.R., Sayer M. and Jen C. K., *Ultrasonics* **39**, Issue 10, 2002, Pages 675-680
5. "Influence of different poling methods on the second-order nonlinearity in fused silica glasses." Xu, Z., Liu, L., Hou, Z., Yang, P., Liu, X., Xu, L., Wang, W., Affatigato M. and Feller S. *Optics Communications* **174**, Issues 5-6, 2000, Pages 475-479
6. "Influence of MgO on the Structural and Electrical Properties of $\text{Bi}_4\text{Ti}_3\text{O}_{12}$ " Sanson, A. and Whatmore R.W., *Integrated Ferroelectrics* 62, Issue 1, 2004 , Pages 193 - 197
7. "Ferroelectric properties of tungsten-doped bismuth titanate thin film prepared by sol-gel route" Kim, J.K., Song, T.K., Kim, S.S. and Kim, J., *Materials Letters* **57**, Issue 4, 2002, Pages 964-968